QILIMANJARO
QUANTUM · TECH

May 2026

Benchmarking Time and Energy in Quantum Simulation: A Comparison of Analog and Digital Approaches

Jan Nogué[1], Josep Bosch[1], Jose Miralles[1], Jordi Riu[1] and Arnau Riera[1]

[1] Qilimanjaro Quantum Tech
Carrer de Veneçuela, 74, Sant Martí, 08019, Barcelona, Spain

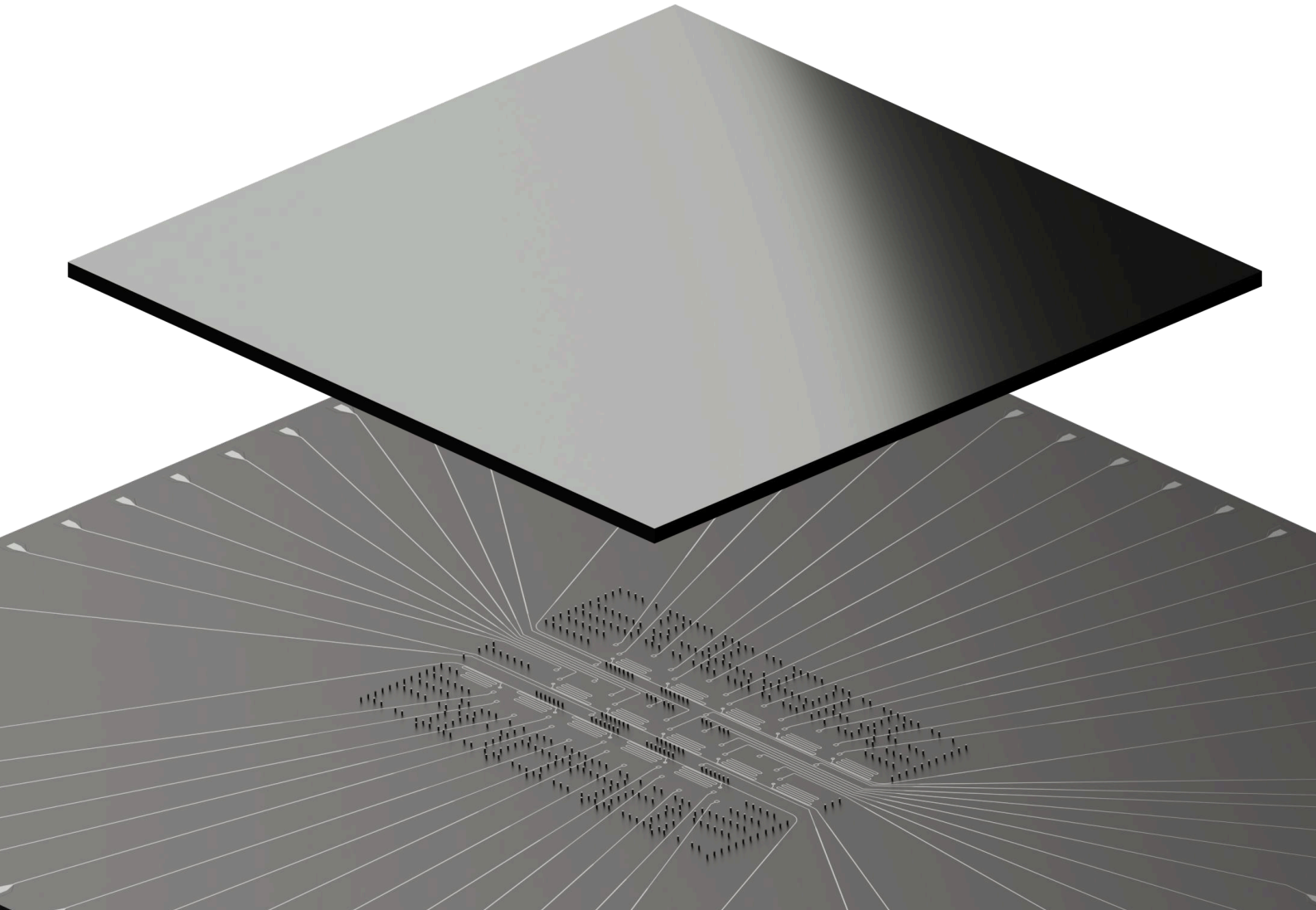

Hamiltonian time evolution is a central primitive in quantum information processing, and a notoriously difficult task for classical computation, making it one of the most compelling candidates for achieving quantum advantage with both digital and analog quantum devices. In this work, we quantitatively compare digital (gate-based) and analog quantum computing platforms using the time evolution of the transverse-field Ising model on a two-dimensional lattice as a simple and representative benchmark.

The analysis considers the time, accuracy, and energy requirements associated with each approach. In gate-based digital quantum simulation, Hamiltonian dynamics are approximated through discrete sequences of quantum gates, typically based on Trotter or related decompositions, leading to circuit depths that grow with the simulated evolution time. Analog quantum simulators, by contrast, realize the target Hamiltonian directly and reproduce its dynamics through continuous-time evolution, thereby avoiding explicit gate decompositions.

Our central finding is that, for the benchmark task considered, *no currently available digital quantum computer* can reproduce the dynamics with the same precision (within a 5% error budget) attainable by an analog quantum computer. The required circuit runtimes exceed multi-qubit coherence times by one to three orders of magnitude, and the implied logical two-qubit error rates are three to six orders of magnitude below current physical two-qubit gate error rates. Thus, accurate digital simulation would require fault-tolerant quantum error correction. Even assuming fault-tolerant logical gates are available, analog quantum computers retain a substantial advantage over their digital counterparts in runtime, energy cost, and economic cost for this class of problems.

Our results indicate that analog quantum computers provide a more resource-efficient implementation of Hamiltonian time evolution, achieving shorter time-to-solution and lower energy cost for a broad class of problems. Although analog quantum hardware does not yet provide the same level of universal programmability as gate-based platforms, it offers practical advantages for applications in quantum simulation, adiabatic and annealing protocols, and quantum reservoir-based machine learning.

Contents

1 Introduction

The controlled implementation of Hamiltonian time evolution is a central task in quantum information science. It underlies a wide range of applications, including the simulation of quantum many-body systems, adiabatic quantum computation, quantum annealing, and emerging approaches to quantum machine learning such as quantum reservoir computing. In many of these settings, the goal is to engineer or approximate the dynamics generated by a target Hamiltonian over a given time interval.

Quantum simulation of many-body systems has long been recognized as one of the most promising applications of quantum computing [1, 2]. More broadly, Hamiltonian dynamics provides a unifying framework to solve problems in physics, chemistry, optimization, and learning. For instance, adiabatic quantum computation and quantum annealing rely on slowly varying Hamiltonians to encode optimization problems, while quantum reservoir computing exploits the natural dynamics of quantum systems to process temporal information.

Analog quantum computers aim to implement a target Hamiltonian directly in hardware and reproduce its dynamics through continuous-time evolution. Because the computation is carried out by the intrinsic physics of the device, this approach avoids the need for decomposing the evolution into discrete operations. Digital quantum computers, by contrast, approximate time evolution using sequences of quantum gates, based either on product-formula methods such as Trotterization or on alternative Hamiltonian-simulation frameworks such as block encoding and qubitization. While universal, these approaches generally introduce significant overhead in circuit depth and gate count.

These differences have motivated a long-standing discussion about the relative merits of analog and digital quantum approaches. Early experimental efforts by D-Wave suggested that large-scale quantum annealers could address certain classes of optimization problems [3, 4], while gate-based platforms pursued by companies such as IBM have emphasized universality and programmability [5, 6]. This distinction reflects a broader trade-off between specialization and generality in quantum computing architectures.

In this context, the absence of an explicit gate decomposition is often viewed as a potential advantage of analog quantum simulation. However, the practical cost of simulation is also shaped by how errors accumulate in each paradigm. In digital quantum simulation, errors are associated with imperfect gates and with the increasing number of operations required to approximate the dynamics. In analog quantum simulation, they are associated with control imperfections and deviations between the implemented and target Hamiltonians.

As a result, while the precise scaling depends on the implementation and hardware properties, the accuracy scaling with system size can be comparable in both paradigms. The key distinction often lies instead in their operational overhead. Digital quantum simulation often requires deep circuits, long execution times, and high-fidelity gates, and achieving scalable high accuracy ultimately relies on quantum error correction, which introduces substantial overhead in qubit count, control complexity, and energy consumption. Analog quantum simulation, in contrast, can realize the same dynamics more directly, reducing both runtime and energy cost.

In this work, we develop a quantitative framework to compare the time, accuracy, and energy requirements of Hamiltonian time evolution across analog quantum devices and digital quantum computers. We analyze digital simulation using Trotter decompositions of first, second, fourth, and sixth order, allowing us to identify the regime in which higher-order formulas cease to improve performance for the benchmark considered here. This highlights a broader challenge in digital simulation, since the optimal Trotter order is generally not known in advance and depends on accuracy requirements, noise levels, and compilation efficiency. We derive optimal resource estimates under realistic noise assumptions and evaluate the resulting circuit depth, runtime,

and energy consumption. We then compare these results with analog quantum simulation and introduce a simple energy model that enables a direct comparison across paradigms.

Our results show that, while the asymptotic scaling of analog and digital quantum simulation is similar, the practical overhead associated with digital approaches, particularly in the fault-tolerant regime, is substantial. This indicates that analog quantum simulators will continue to play an important role for a broad class of dynamical problems, even as digital quantum computing matures.

2 Digital Simulation of a Time Evolution: Product Formulas

Consider the time evolution generated by a Hamiltonian H,

$$U(t) = e^{-iHt}. \tag{1}$$

In many physical systems, the Hamiltonian can be decomposed into a sum of terms

$$H = \sum_{j=1}^{m} H_j, \tag{2}$$

where each H_j corresponds to a local interaction that can be easily implemented in a quantum circuit. If all H_j commute, the time evolution factorizes exactly,

$$e^{-iHt} = \prod_{j=1}^{m} e^{-iH_j t}. \tag{3}$$

However, in general the terms do not commute, and the evolution must be approximated. Product formulas, also known as Trotter–Suzuki decompositions, achieve this by splitting the evolution into r small time steps of size $\Delta t = t/r$ and applying a structured sequence of partial evolutions at each step [7, 8].

2.1 First-Order Trotter (Lie–Trotter Formula)

The simplest product formula approximates the evolution as

$$U(t) \approx S_1(t/r)^r, \qquad S_1(\Delta t) = \prod_{j=1}^{m} e^{-iH_j \Delta t}. \tag{4}$$

Using the Baker–Campbell–Hausdorff (BCH) expansion, one can show that each step introduces an error proportional to the commutators of the Hamiltonian terms. For a Hamiltonian split into two non-commuting parts $H = A + B$:

$$e^{-iA\Delta t}\, e^{-iB\Delta t} = e^{-i(A+B)\Delta t - \frac{\Delta t^2}{2}[A,B] + \mathcal{O}(\Delta t^3)}. \tag{5}$$

The first-order Trotter error therefore satisfies the bound

$$\left\| S_1(t/r)^r - e^{-iHt} \right\| \leq \frac{t^2}{2r} \sum_{j<k} \|[H_j, H_k]\| + \mathcal{O}\left(\frac{t^3}{r^2}\right). \tag{6}$$

The error per step scales as $\mathcal{O}(\Delta t^2)$, and the total error after r steps scales as

$$\epsilon^{(1)}_{\text{Trotter}} = \mathcal{O}\left(\frac{t^2}{r}\right). \tag{7}$$

2.2 Second-Order Suzuki–Trotter

Higher accuracy is obtained by symmetrizing the splitting. For $H = A + B$, the second-order formula reads

$$S_2(\Delta t) = e^{-iA\,\Delta t/2}\, e^{-iB\,\Delta t}\, e^{-iA\,\Delta t/2}. \tag{8}$$

The symmetry of this construction ensures that the even powers of Δt vanish in the BCH expansion (Δt^2, $\Delta t^4 \ldots$). The surviving error is at order Δt^3:

$$\|S_2(\Delta t) - e^{-iH\Delta t}\| \leq \frac{\Delta t^3}{12}\,\alpha_2 + \mathcal{O}(\Delta t^5), \tag{9}$$

where the error coefficient α_2 involves nested double commutators of the Hamiltonian terms (see Appendix B for the full derivation):

$$\alpha_2 = \|[B,[B,A]]\| + \tfrac{1}{2}\|[A,[A,B]]\|. \tag{10}$$

After r steps, the total Trotter error is bounded by

$$\epsilon^{(2)}_{\text{Trotter}} \leq \frac{\alpha_2\, t^3}{12\, r^2}. \tag{11}$$

The key advantage is the improved scaling: the error now decreases as Δt^2 rather than Δt, allowing far fewer steps for the same accuracy.

2.3 Fourth-Order Suzuki–Trotter

Suzuki [8] showed that higher-order formulas can be built *recursively* from lower-order ones. The fourth-order formula is constructed from five applications of S_2:

$$S_4(\Delta t) = S_2(s_1\Delta t)\; S_2(s_1\Delta t)\; S_2(s_0\Delta t)\; S_2(s_1\Delta t)\; S_2(s_1\Delta t), \tag{12}$$

where the parameters are chosen to cancel the third-order error:

$$s_1 = \frac{1}{4 - 4^{1/3}} \approx 0.4146, \qquad s_0 = 1 - 4s_1 \approx -0.6585. \tag{13}$$

Note that $s_0 < 0$: one of the five S_2 sub-steps runs *backwards in time*. The coefficients satisfy both the consistency condition $4s_1 + s_0 = 1$ and the cancellation condition $4s_1^3 + s_0^3 = 0$, which eliminates the leading third-order error and leaving a surviving error of order $\mathcal{O}(\Delta t^5)$.

After r steps, the total error is bounded by

$$\epsilon^{(4)}_{\text{Trotter}} \leq \frac{\alpha_4\, t^5}{r^4}, \tag{14}$$

where α_4 is a linear combination of norms of all depth-4 nested commutators of the Hamiltonian terms (see Appendix C).

2.4 Sixth-Order Suzuki-Trotter

The sixth-order symmetric formula is built recursively from S_4:

$$S_6(\tau) \;=\; S_4(s_3\tau)^2\, S_4(s_0'\,\tau)\, S_4(s_3\tau)^2, \tag{15}$$

with the two real parameters s_3 and s_0' fixed by the consistency condition ($4s_1 + s_0 = 1$) and the requirement that the order-5 error term cancels out ($4\,s_3^5 + (1 - 4s_3)^5 \;=\; 0$)

$$s_3 \;=\; \frac{1}{4 - 4^{1/5}} \;\approx\; 0.37304, \qquad s_0' \;=\; 1 - 4s_3 \;\approx\; -0.49217. \tag{16}$$

Note that $s_0' < 0$: one of the five S_4-blocks is propagated backward in time, exactly as in the order-4 case where $1 - 4s_1 \approx -0.66$. Because S_6 is symmetric under $\tau \mapsto -\tau$, the Baker–Campbell–Hausdorff expansion of $\ln S_6(\tau)$ contains only odd powers of τ, and Eq. (16) additionally kills the τ^5 term. The leading non-zero correction is therefore at τ^7 and we write

$$\left\| S_6(\tau) - e^{-iH\tau} \right\|_{\text{op}} \leq \alpha_6 \tau^7, \qquad \epsilon^{(6)}_{\text{Trotter}} \leq \frac{\alpha_6 t^7}{r^6}. \tag{17}$$

2.5 Error Per Step vs. Number of Steps

The pattern generalises to product formulas of order p, including the first-order formula and even-order Suzuki formulas. If the error per step scales as $\epsilon_{\text{step}} \sim \alpha_p \Delta t^{p+1}$ and each step requires G_p gates, then the total error after r steps is

$$\epsilon_{\text{Trotter}} \sim \frac{\alpha_p t^{p+1}}{r^p}. \tag{18}$$

Setting this equal to the error budget η determines the required number of steps:

$$r_p^* = \left\lceil \left(\frac{\alpha_p t^{p+1}}{\eta} \right)^{1/p} \right\rceil. \tag{19}$$

The total gate count is then

$$N_{\text{total}} = G_p \cdot r_p^* = G_p \left\lceil \left(\frac{\alpha_p t^{p+1}}{\eta} \right)^{1/p} \right\rceil. \tag{20}$$

Where G_p is the gate per step and is calculated recursively from the base case S_2 (order two). The recursion [8] reads, for $k \geq 2$

$$G_{2k} = 5G_{2k-2} = 5^{k-1} G_2, \;\; G_2 \sim 2m, \;\; p = 2k, \tag{21}$$

therefore

$$G_{2k} \sim 2m5^{k-1}. \tag{22}$$

Here m denotes the number of terms in the Hamiltonian decomposition. The following table summarises the scaling:

Order p	**Error scaling**	**Steps** $r^* \propto$	**Gates/step** $G_p \propto$
1	t^2/r	η^{-1}	m
2	t^3/r^2	$\eta^{-1/2}$	$2m$
4	t^5/r^4	$\eta^{-1/4}$	$10m$
6	t^7/r^6	$\eta^{-1/6}$	$50m$

As p increases, G_p grows exponentially in p, competing against the exponent $1/p$ in r_p^*. This competing effect makes it such that, for a given problem, increasing the Trotter order decreases the total number of gates until reaching a minimum. After that, the number of gates increases with the Trotter order. This means that, for a given Hamiltonian, there is an optimal Trotter order for a given error budget.

We can see this intuitively using Eq.20. As $p \to \infty : t^{1+1/p} \to t$ and $\eta^{-1/p} \to 1$ and $\alpha_p^{1/p}$

approaches a constant of order $||H||$ (since α_p depends on depth $p+1$ nested commutators that are bounded by $2||H||)^{p+1}$. So r^* saturates at a finite floor. Putting this together

$$\lim_{p\to\infty} N_{\text{total}}(p) \sim 5^{p/2} \times ||H||tm \to \infty \tag{23}$$

Therefore, the total gate count does not decrease monotonically with p and there exists a tradeoff instead. To broadly estimate the optimal p for our benchmark, we can minimize $\ln N_{total}(p) \approx p/2 \ln 5 + 1/p \ln(Ct/\eta) + \text{const}$

$$p^* \approx \sqrt{\frac{2\ln(||H||t/\eta)}{\ln 5}} \tag{24}$$

For the 5×5 lattice, $Jt = ht = 10, \eta = 0.05$, $||H||t \sim J|E| + h|V| \sim 650 \to p^* \approx 3.5$

3 Error in the Digital Simulation of Time Evolution

A real quantum computer has many sources of errors, from state preparation, to measurement, control of the qubits, among others. In this analysis we do not model all physical error sources explicitly, as they will be different in analog and digital. Instead, we focus on two relevant contributions: the errors coming from the algorithm itself and the error associated with the imperfect gates implementation:

$$\boxed{\epsilon_{\text{total}} \leq \epsilon_{\text{Trotter}} + \epsilon_{\text{gates}}.} \tag{25}$$

- $\epsilon_{\text{Trotter}}$: the discretisation error from approximating e^{-iHt} by a product formula. This is an *algorithmic* error, intrinsic to the product-formula approximation itself, and is therefore present even in the ideal limit of noiseless gates. **Decreases** with more steps.
- ϵ_{gates}: the errors due to imperfect gate implementations. Each gate introduces a small error, and these accumulate. **Increases** with more steps.

These two contributions pull in opposite directions:

	More steps	**Fewer steps**
Trotter error	↓ decreases	↑ increases
Gates error	↑ increases	↓ decreases

3.1 General Error Framework

For a product formula of order p, let N_{2q}^{step} and N_{1q}^{step} denote the number of two-qubit and single-qubit gates per Trotter step, respectively. Let ϵ_{2q} and ϵ_{1q} denote the corresponding per-gate error rates, assumed small, stochastic, uncorrelated and in a first-order approximation. After r steps:

$$\epsilon_{\text{Trotter}} \sim \frac{\alpha_p\, t^{p+1}}{r^p}, \tag{26}$$

$$\epsilon_{\text{gates}} = r\big(N_{2q}^{\text{step}}\,\epsilon_{2q} + N_{1q}^{\text{step}}\,\epsilon_{1q}\big). \tag{27}$$

Defining the effective per-step gate noise as $\gamma = N_{2q}^{\text{step}}\,\epsilon_{2q} + N_{1q}^{\text{step}}\,\epsilon_{1q}$, the total error becomes

$$\epsilon_{\text{total}}(r) = \frac{\alpha_p\, t^{p+1}}{r^p} + \gamma\, r. \tag{28}$$

3.2 Optimal Number of Trotter Steps

The total error exhibits a characteristic U-shaped dependence on r: for small r the Trotter error dominates, while for large r the gate errors dominate. The minimum is found by differentiating Eq. (28):

$$r^* = \left(\frac{p\,\alpha_p\,t^{p+1}}{\gamma} \right)^{1/(p+1)}. \tag{29}$$

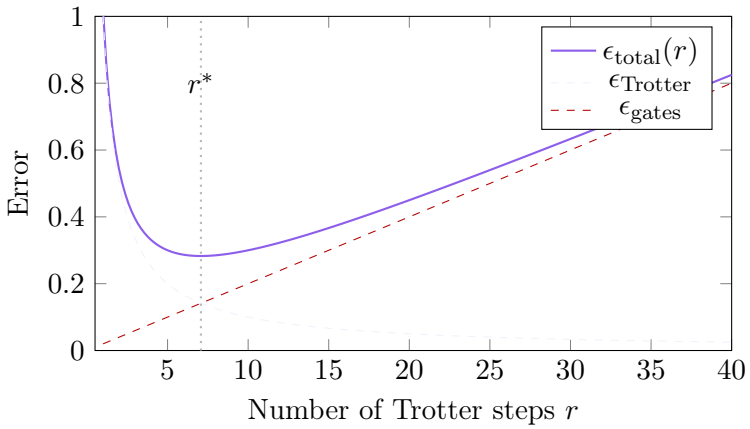

Figure 1: Trade-off between Trotter error and accumulated gate noise in digital quantum simulation. The total error exhibits a minimum at the optimal value r^*.

3.3 Minimum Achievable Error

Substituting r^* into Eq. (28) yields the minimum achievable error for a given set of hardware parameters. For the first-order formula ($p = 1$) one obtains the closed-form result

$$\epsilon^{(1)}_{\text{min}}(t) = 2t\sqrt{\alpha_1\,\gamma}, \tag{30}$$

which shows that even under optimal conditions the achievable accuracy deteriorates linearly with the simulated time. For higher orders, the minimum error takes the general form

$$\epsilon^{(p)}_{\text{min}}(t) \propto t\ \ (\alpha_p)^{1/(p+1)}\ \ \gamma^{p/(p+1)}. \tag{31}$$

Higher-order formulas reduce the exponent of the Trotter error coefficient α_p and increase the exponent of the per-step gate noise γ, while remaining linear in t for all p.

3.4 Splitting the Error Budget

Given a total error budget η, we use a simple heuristic to split evenly between the two contributions. Setting $\epsilon_{\text{Trotter}} = \eta/2$ and $\epsilon_{\text{gates}} = \eta/2$, the Trotter error budget determines the number of steps r^*_p as in Section 2, while the gate budget gives a constraint on the required gate fidelities

$$\boxed{\epsilon_{1q} \leq \frac{\eta}{2\,r^*_p\,(\kappa\,N^{\text{step}}_{2q} + N^{\text{step}}_{1q})}, \qquad \epsilon_{2q} = \kappa\,\epsilon_{1q},} \tag{32}$$

where $\kappa = \epsilon_{2q}/\epsilon_{1q}$ is the two-qubit to single-qubit gate error ratio, typically $\kappa \approx 10$ for superconducting qubits [9–14].

4 Benchmark: Transverse-Field Ising Model

To make the preceding analysis concrete, we apply it to the transverse-field Ising model on a graph $G = (V, E)$, a paradigmatic model in quantum simulation and condensed matter physics [15].

4.1 Hamiltonian

$$H = \underbrace{J \sum_{(i,j)\in E} Z_i Z_j}_{H_{ZZ}} + \underbrace{h \sum_{i\in V} X_i}_{H_X} = H_{ZZ} + H_X. \tag{33}$$

The two terms do not commute, $[H_{ZZ}, H_X] \neq 0$, making this a non-trivial test case for product-formula decompositions.

4.2 Gate-Level Implementation of One Trotter Step

Since all $Z_i Z_j$ terms commute with each other:

$$e^{-iH_{ZZ}\,\Delta t} = \prod_{(i,j)\in E} e^{-iJ\Delta t\, Z_i Z_j}. \tag{34}$$

Using the standard convention $R_z(\phi) := e^{-i\phi Z/2}$, $R_x(\phi) := e^{-i\phi X/2}$, each two-body factor is implemented as

$$e^{-iJ\Delta t\, Z_i Z_j} = \mathrm{CNOT}_{i,j} \cdot R_z(2J\Delta t)_j \cdot \mathrm{CNOT}_{i,j}, \tag{35}$$

costing **2 CNOT gates + 1 single-qubit R_z rotation by angle** $2J\Delta t$ per edge. Since all X_i terms commute:

$$e^{-iH_X\,\Delta t} = \prod_{i\in V} R_x(2h\Delta t)_i, \tag{36}$$

costing $|V|$ **single-qubit R_x rotations by angle** $2h\Delta t$ and zero two-qubit gates. The Trotter step size Δt therefore controls every rotation angle in the circuit linearly: halving Δt halves each R_z and R_x angle (and doubles the number of repetitions).

4.3 Parallelisation via Edge Colouring

The $|E|$ two-qubit gates in $e^{-iH_{ZZ}\,\Delta t}$ cannot all run simultaneously (gates on edges sharing a qubit conflict). An edge colouring partitions E into $\chi'(G)$ groups of non-conflicting edges, where $\chi'(G)$ is the chromatic index of the graph. Gates within each group run in parallel. The circuit depth of one ZZ layer is therefore $2\chi'(G)t_{2q} + \chi'(G)t_{1q}$, while the X layer depth is just t_{1q}.

4.4 Gate Counts Per Trotter Step

Order	ZZ layers	X layers	N_{2q}^{step}	N_{1q}^{step}	Step duration
S_1	1	1	$2\|E\|$	$\|E\| + \|V\|$	$2\chi' t_{2q} + (\chi' + 1)t_{1q}$
S_2	2	1	$4\|E\|$	$2\|E\| + \|V\|$	$4\chi' t_{2q} + (2\chi' + 1)t_{1q}$
S_4	10	5	$20\|E\|$	$10\|E\| + 5\|V\|$	$20\chi' t_{2q} + (10\chi' + 5)t_{1q}$
S_6	50	25	$100\|E\|$	$50\|E\| + 25\|V\|$	$100\,\chi' t_{2q} + (50\chi' + 25)\,t_{1q}$

The fourth-order formula requires $5\times$ more S_2 sub-steps, each consisting of 2 ZZ layers and 1 X layer.

4.5 Trotter Error Coefficients

The Trotter error coefficients for this Hamiltonian depend on the commutator norms of H_{ZZ} and H_X.

First-order coefficient α_1. The commutator $[H_{ZZ}, H_X] = 2iJh \sum_{(i,j)\in E}(Y_iZ_j + Z_iY_j)$ yields

$$\alpha_1 := \|[H_{ZZ}, H_X]\| \leq 4|Jh|\,|E|. \tag{37}$$

Second-order coefficient α_2. The nested double commutators give (Appendix B):

$$\alpha_2 \leq 4|Jh|\,|E|\,(4|h| + |J|\,d_{\max}), \tag{38}$$

where $d_{\max}$ is the maximum vertex degree of G.

Fourth-order coefficient α_4. The resulting upper bound is a sum of fifth-order terms in J and h, with graph-dependent factors controlled by $|E|$ and powers of $d_{\max}$. The full expression depends on the combinatorial coefficients from the BCH expansion of S_4. See Appendix C for the complete derivation.

Sixth-order coefficient α_6. The depth-6 generator E_7 in $\ln S_6(\tau)$ involves $2^6 = 64$ nested commutator patterns, making the full analytical derivation of the bound hard. In this case, instead of deriving the analytical bound, we approximate α_6 by direct numerical fitting of Eq. (17) on a small reference lattice and rescale to the target chips by extensivity. The procedure to approximate α_6 is described in Appendix D.

4.6 Chip Topologies

We evaluate all formulas on three chip topologies representative of Qilimanjaro's upcoming devices:

Chip	Topology	$\lvert V\rvert$	$\lvert E\rvert$	$d_{\max}$	$\chi'(G)$
Phoenix-15	5×3 hexagonal	15	22	3	3
Phoenix-16	4×4 square	16	24	4	4
Phoenix-25	5×5 square	25	40	4	4

4.7 Benchmark Parameters

Symbol	Meaning	Value	Note
J, h	Coupling strengths	10	μs^{-1} ($Jt = ht = 10$)
t	Evolution time	1	Physical: 1 μs
η	Total error budget	0.05	5%
κ	Gate error ratio	10	$\epsilon_{2q}/\epsilon_{1q}$
t_{2q}	Two-qubit gate time	50 ns	
t_{1q}	Single-qubit gate time	5 ns	

4.8 Numerical Results: Steps and Gate Counts

Using the error coefficients computed above and setting $\epsilon_{\text{Trotter}} = \eta/2 = 0.025$, the required number of steps for each order and topology follows from the error bound $\epsilon^{(p)}_{\text{Trotter}} \leq \eta/2$:

$$p = 1: \quad \frac{\alpha_1 t^2}{2r} \leq \frac{\eta}{2} \implies r_1^* = \left\lceil \frac{\alpha_1 t^2}{\eta} \right\rceil, \tag{39}$$

$$p = 2: \quad \frac{\alpha_2 t^3}{12 r^2} \leq \frac{\eta}{2} \implies r_2^* = \left\lceil \sqrt{\frac{\alpha_2 t^3}{6\eta}} \right\rceil, \tag{40}$$

$$p = 4: \quad \frac{\alpha_4 t^5}{r^4} \leq \frac{\eta}{2} \implies r_4^* = \left\lceil \left(\frac{2\alpha_4 t^5}{\eta} \right)^{1/4} \right\rceil. \tag{41}$$

$$p = 6: \quad \frac{\alpha_6 t^7}{r^6} \leq \frac{\eta}{2} \implies r_6^* = \left\lceil \left(\frac{2\alpha_6 t^7}{\eta} \right)^{1/6} \right\rceil. \tag{42}$$

Table 1: First-order Trotter: $r_1^* = \lceil \alpha_1 t^2/\eta \rceil$ (from Eq. 39).

Chip	α_1	r_1^*	$G_1^{(2q)}$	$N_{2q}^{(1)}$	Runtime
5×3 hex	8 800	176 000	44	7.74 M	56.32 ms
4×4 sq	9 600	192 000	48	9.22 M	81.60 ms
5×5 sq	16 000	320 000	80	25.6 M	136 ms

Table 2: Second-order Trotter: $r_2^* = \lceil \sqrt{\alpha_2 t^3/(6\eta)} \rceil$ (from Eq. 40).

Chip	α_2	r_2^*	$G_2^{(2q)}$	$N_{2q}^{(2)}$	Runtime
5×3 hex	6.16×10^5	1 433	88	126 K	0.91 ms
4×4 sq	7.68×10^5	1 600	96	154 K	1.35 ms
5×5 sq	1.28×10^6	2 066	160	331 K	1.75 ms

Table 3: Fourth-order Trotter: $r_4^* = \lceil (2\alpha_4 t^5/\eta)^{1/4} \rceil$ (from Eq. 41).

Chip	α_4	r_4^*	$G_4^{(2q)}$	$N_{2q}^{(4)}$	Runtime
5×3 hex	3.28×10^6	108	440	48 K	0.34 ms
4×4 sq	7.12×10^6	131	480	63 K	0.55 ms
5×5 sq	1.19×10^7	148	800	120 K	0.63 ms

Table 4: Sixth-order Trotter: $r_6^* = \lceil (2\alpha_6 t^7/\eta)^{1/6} \rceil$ (from Eq. 42).

Chip	α_6	r_6^*	$G_6^{(2q)}$	$N_{2q}^{(6)}$	Runtime
5×3 hex	$\sim 7.34 \times 10^7$	38	2200	84 K	0.60 ms
4×4 sq	$\sim 8 \times 10^7$	39	2400	94 K	0.82 ms
5×5 sq	$\sim 1.34 \times 10^8$	42	4000	168 K	0.89 ms

From these numerical results we see that, for all three topologies, increasing the order from S_1 to S_4 reduces both the required number of Trotter steps and the total two-qubit gate count. This trend reverses at S_6: although r^* continues to decrease (from $r_4^* = 148$ to $r_6^* = 42$ on the 5×5 lattice), the growth of per-step gates $G_6 = 5\,G_4$ outweighs the reduction in steps, so the total two-qubit count grows and the circuit runtime becomes longer. Fourth order is therefore the practical optimum for this benchmark, in agreement with the estimate $p^* \approx 3.5$ derived in Section 2.5. Pushing to S_6 and to higher even orders produces *more* gates and a *longer* circuit, not fewer and shorter, even though each individual step is more accurate.

We conclude that this is a structural limitation of *product-formula* simulation with Trotter: for any given problem and error budget there is a finite optimal order p^*, beyond which the exponential growth of per-step gates dominates over the diminishing returns in the number of steps.

4.9 Current Hardware Limitations

The preceding analysis determines the *theoretically optimal* number of Trotter steps and the resulting circuit runtimes. However, these figures must be compared against the physical constraints of existing quantum hardware: finite qubit coherence times and accumulated hardware noise per Trotter step.

State-of-the-art superconducting transmon processors exhibit typical coherence times $T_2 \sim 50$–$200\,\mu$s in multi-qubit devices [9, 16]. Recent materials advances have pushed single-qubit coherence beyond 1 ms in isolated devices [17], but these figures have not yet been replicated in multi-qubit processors.
Comparing these timescales with the circuit runtimes computed above for the 5×5 lattice reveals a gap:

Order	**Circuit runtime**	**Typical T_2**	**Ratio (runtime/T_2)**
S_1	136 ms	100 μs	$\sim 1360\times$
S_2	1.75 ms	100 μs	$\sim 18\times$
S_4	0.63 ms	100 μs	$\sim 6\times$
S_6	0.89 ms	100 μs	$\sim 9\times$

All four decompositions require circuit execution times that exceed typical multi-qubit coherence times by one to three orders of magnitude. In practice, the execution would lead to strong decoherence and accumulated gate noise, suppressing almost completely the useful signal in the quantum state regardless of the product-formula order.

An equally important limitation concerns the *per-step hardware noise* $\gamma = N_{2q}^{\text{step}}\,\epsilon_{2q} + N_{1q}^{\text{step}}\,\epsilon_{1q}$ introduced in Section 3.1. Higher-order formulas reduce the number of steps r^*, but they achieve this by packing *more gates into each step*. With current two-qubit gate error rates $\epsilon_{2q} \sim 10^{-3}$ [16, 18–21], the per-step noise for the 5×5 lattice is:

Table 5: Accumulated gate-noise estimates for the 5×5 lattice using $\epsilon_{2q} = 10^{-3}$ and $\epsilon_{1q} = 10^{-4}$.

Order	N_{2q}^{step}	N_{1q}^{step}	r^*	γ_{SOTA}	$r^*\gamma_{SOTA}$
S_1	80	65	320000	~ 0.087	$\sim 2.8 \times 10^4$
S_2	160	105	2066	~ 0.171	$\sim 3.5 \times 10^2$
S_4	800	525	148	~ 0.853	$\sim 1.3 \times 10^2$
S_6	4000	2625	42	~ 4.26	$\sim 1.8 \times 10^2$

Here we used $\epsilon_{2q} = 10^{-3}$ and $\epsilon_{1q} = 10^{-4}$ as representative values. The relevant quantity to compare against the budget η is the accumulated gate-error estimate over the full circuit, $r^*\gamma$, shown in the last column of Table 5. For all four orders this quantity lies between $\sim 10^2$ and $\sim 10^4$, i.e. three to six orders of magnitude above $\eta = 0.05$. On current hardware, the operating point $r^* \gg 1$ at which the Trotter error is acceptably small lies far beyond the regime where the first-order gate-noise model remains perturbative, let alone kept below threshold.

The crossover at which higher-order formulas become advantageous therefore requires gate fidelities several orders of magnitude beyond the current state of the art, as quantified in the next section.

5 Gate Fidelity Requirements

Part of what makes analog quantum simulation attractive is that it avoids the deep circuits and restrictive gate-fidelity requirements of the digital approach. In this section we quantify those requirements for each product formula order. In Table 6 we calculate the required single- and two-qubit gate error $(\epsilon_{1q}, \epsilon_{2q})$ to maintain a $\eta = 5\%$ error for the 5x5 lattice and in Table 7 we extend the calculation of ϵ_{2q} for the other geometries.

Table 6: Required gate fidelities for 5% total simulation error (5×5 lattice). Constraints on *both* single and two-qubit gates. The budget split is $\epsilon_{\text{Trotter}} = \epsilon_{\text{gates}} = \eta/2$, with $\kappa = \epsilon_{2q}/\epsilon_{1q} = 10$.

Order	r^*	N_{1q}^{tot}	N_{2q}^{tot}	**Req.** ϵ_{1q}	**Req.** ϵ_{2q}
1st-order	320 000	20.8 M	25.6 M	9.0×10^{-11}	9.0×10^{-10}
2nd-order	2 066	216.9 K	330.6 K	7.1×10^{-9}	7.1×10^{-8}
4th-order	148	77.7 K	118.4 K	2.0×10^{-8}	2.0×10^{-7}
6th-order	42	110.2 K	168.0 K	1.4×10^{-8}	1.4×10^{-7}
SOTA [16, 18–21]				$\sim 10^{-4}$	$\sim 10^{-3}$

Table 7: Required two-qubit gate error ϵ_{2q} to achieve 5% total error, across orders and topologies.

Chip	**1st order**	**2nd order**	**4th order**	**6th order**
5×3 hex	3.0×10^{-9}	1.9×10^{-7}	4.9×10^{-7}	2.8×10^{-7}
4×4 sq	2.5×10^{-9}	1.5×10^{-7}	3.7×10^{-7}	2.5×10^{-7}
5×5 sq	9.0×10^{-10}	7.1×10^{-8}	2.0×10^{-7}	1.4×10^{-7}

A fourth-order Trotter decomposition requires $\epsilon_{2q} \sim 10^{-7}$ compared to $\sim 10^{-9}$–10^{-10} for first order, an improvement of $\sim$ 100–1 000×. But the gap to state-of-the-art hardware remains **three to seven orders of magnitude** for two qubit gates and **four to eight orders of magnitude** for single qubit gates. Our analysis shows that achieving high-accuracy digital simulation of quantum dynamics is out of reach for current NISQ hardware and will require quantum error correction, which introduces substantial overhead in qubit count, circuit depth, and execution time.

6 Energy Consumption: Analog vs. Digital

The preceding sections have established that, for the given benchmark and error budgets, accurate digital simulation of Hamiltonian dynamics via product formulas, regardless of the order, is unattainable on current NISQ hardware since the required circuit runtimes exceed qubit coherence times by orders of magnitude, and the necessary gate fidelities surpass the state of the art by three to seven orders of magnitude. Reaching the operating regime where digital simulation becomes viable will therefore require fault-tolerant quantum computation.

In this section, we *assume* that fault-tolerant digital quantum computers are available, with gates of sufficient fidelity to execute the full Trotterised circuits derived in Section 4. In doing so we *ignore* the two principal overheads of fault tolerance: (i) the large factor in physical-qubit count required per logical qubit by any quantum error-correcting code, and (ii) the per-gate cost of the error-correction protocol itself, which adds latency and energy to every logical operation. Both would only widen the analog–digital gap, so the comparison below should be read as a *lower bound* on the true digital cost in a fault-tolerant setting.

Under this assumption, we compare the energy consumption of analog and digital approaches. Our aim is to show that, even when the fidelity bottleneck is removed, analog quantum simulators retain a substantial advantage over their digital counterparts in runtime, energy cost, and direct economic cost. The dominant energy contribution in both paradigms arises from the cryogenic cooling infrastructure and classical control electronics, which draw power continuously throughout the computation.

6.1 General Energy Model

The total energy consumed by a quantum experiment can be written as

$$E_{\text{system}} = P_{\text{system}} \times T_{\text{experiment}}, \tag{43}$$

where P_{system} is the average power draw of the full stack (cryogenics and supporting electronics), and $T_{\text{experiment}}$ is the total time required to perform the computation. This assumes that P_{system} is approximately constant throughout a shot, which is valid for always-on cryogenic systems.

6.2 Analog Quantum Computing

In an analog quantum device, the evolution is implemented by engineering a target Hamiltonian $\hat{H}(t)$ and allowing the system to evolve continuously for a time t_{evol}:

$$E_{\text{analog}} = P_{\text{system}} \times N_{\text{shots}} \times (t_{\text{reset}} + t_{\text{evol}} + t_{\text{meas}}), \tag{44}$$

where N_{shots} is the number of experimental repetitions, t_{reset} is the qubit initialisation time, t_{evol} is the duration of the quantum evolution, and t_{meas} is the measurement and readout time. Because no discrete gate decomposition is required, the evolution time is set directly by the physical timescale of the simulated problem.

6.3 Digital (Gate-Based) Quantum Computing

For a gate-based processor implementing a Trotter decomposition of order p, the evolution consists of r_p^* structurally identical Trotter steps, each of duration $t_{\text{step}}^{(p)}$ given in Section 4:

$$t_{\text{step}}^{(p)} = N_{2q}^{\text{layers}}\,\chi'(G)\,t_{2q} + N_{1q}^{\text{layers}}\,t_{1q}, \tag{45}$$

where N_{2q}^{layers} and N_{1q}^{layers} count the parallelised two-qubit and single-qubit layers per Trotter step, and $\chi'(G)$ is the chromatic index of the interaction graph. The total energy for N_{shots} repetitions is then

$$E_{\text{digital}}^{(p)} = P_{\text{system}}\,N_{\text{shots}}\left(t_{\text{reset}} \;+\; r_p^*\,t_{\text{step}}^{(p)} \;+\; t_{\text{meas}}\right). \tag{46}$$

For deep circuits, as required by Trotter decompositions, the term $r_p^*\,t_{\text{step}}^{(p)}$ dominates over reset and readout; because $t_{\text{step}}^{(p)}$ is itself dominated by the two-qubit contribution $\propto \chi'(G)\,t_{2q}$ (since $t_{2q} \gg t_{1q}$ on superconducting hardware), the two-qubit gate speed is the primary lever for reducing energy per shot.

6.4 Comparative Analysis

We perform the comparison for the 5×5 lattice benchmark with $t_{\text{evol}} = 1\,\mu\text{s}$, $N_{\text{shots}} = 20\,000$, and $P_{\text{system}} = 19\,\text{kW}$, the energy cost for each paradigm and Trotter order is summarised in Table 8.[1]

Table 8: Energy consumption comparison for the 5×5 lattice benchmark. Parameters: $t_{\text{reset}} = 5\,\mu\text{s}$, $t_{\text{meas}} = 1\,\mu\text{s}$, $P_{\text{sys}} = 19\,\text{kW}$, $N_{\text{shots}} = 20\,000$.

Method	T_{shot}	T_{total}	E_{total}	**kWh**	**Ratio vs. analog**
Analog	$7\,\mu\text{s}$	0.14 s	2.66 kJ	7.4×10^{-4}	1×
6th-order	0.89 ms	17.9 s	339 kJ	0.094	128×
4th-order	0.63 ms	12.6 s	240 kJ	0.067	90×
2nd-order	1.75 ms	35.0 s	666 kJ	0.185	250×
1st-order	136.0 ms	2 720 s	51 682 kJ	14.4	19 429×

The analog approach achieves the lowest energy cost by a factor of ∼90–19 400 depending on the Trotter order. This hierarchy follows directly from the runtime analysis of Section 4: we assume that the cryostat draws the same 19 kW regardless of whether the computation is analog or digital; what differs is *how long* it must run. The analog device completes each shot in $7\,\mu\text{s}$, whereas even the most compact digital decomposition (fourth-order Trotter) requires $631\,\mu\text{s}$, roughly 90× longer, to reproduce the same dynamics.

Going from first to second order reduces the runtime by a factor of ∼78× (from 136 ms to 1.75 ms), and the fourth-order formula achieves a further ∼2.8× reduction (to 0.63 ms). The trend reverses at sixth order: $r_6^* = 42$ is smaller than $r_4^* = 148$, but the per-step gate count grows by a factor of five ($G_6 = 5G_4$), so the total runtime *increases* from 0.63 ms to 0.89 ms and the energy cost grows from 240 kJ to 339 kJ. Fourth order is the sweet spot, and pushing beyond it costs both runtime *and* energy.

[1] Full derivations of all numerical values in this section are given in Appendix E.

6.5 Electricity Cost

The energy differences translate into direct electricity-cost differences. At a US average retail electricity price of \$0.14/kWh (2025) [22]:

Table 9: Electricity cost per full experiment (5×5 lattice, 20 000 shots, $\eta = 5\%$ total error). US 2025 average retail price \$0.14/kWh.

Method	**Energy (kWh)**	**Electricity cost**
Analog	7.4×10^{-4}	$<$ \$0.01
4th-order Trotter	0.067	$<$ \$0.01
6th-order Trotter	0.094	$<$ \$0.02
2nd-order Trotter	0.185	\$0.03
1st-order Trotter	14.4	\$2.01

The analog approach costs less than one cent per experiment. Fourth-order Trotter also costs less than one cent, only 90× the analog energy, making it economically viable for individual experiments in isolation. Sixth-order is slightly more expensive but still under two cents. The second-order cost is modest at ∼\$0.03 per experiment. Only first-order Trotter incurs a non-trivial electricity cost (∼\$2.01), which, while affordable for a single run, would accumulate to ∼\$2 000 for 1 000 independent parameter sweeps.

It should be emphasised that these electricity costs account only for the energy consumed during the quantum computation itself. In practice, the dilution refrigerator draws power continuously (not only during shots), and additional overhead arises from classical pre- and post-processing. The figures above therefore represent a *lower bound* on the true operational cost, but they capture the correct *relative* differences between paradigms, since all approaches share the same cryogenic baseline.

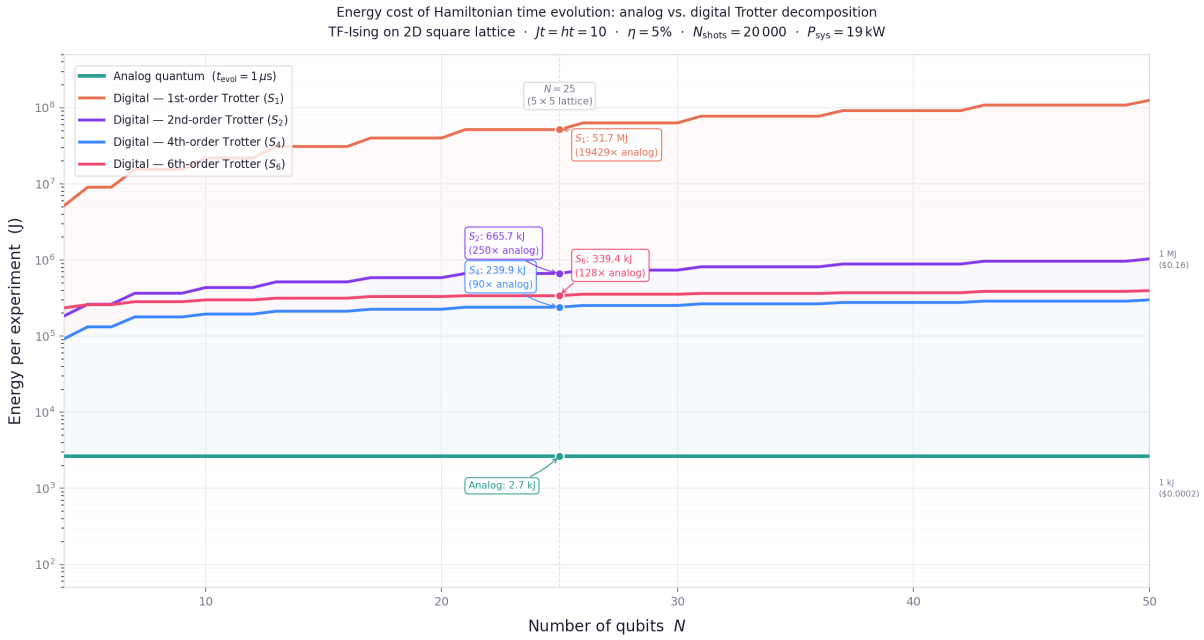

Figure 2: Energy cost per full experiment as a function of system size N for a two-dimensional square lattice. The analog energy cost (horizontal line) is independent of N. Digital energy costs grow as $N^{1/p}$ for pth-order Trotter, reflecting the scaling of the error coefficients with the number of edges $|E| \propto N$. The analog advantage widens with system size for all orders.

6.6 Scaling with System Size

Unlike the analog energy cost, which is independent of the number of qubits N (the evolution time t_{evol} is set by the physics of the problem, not by the hardware), the digital energy cost grows with N.

For a two-dimensional square lattice with $N = L^2$ qubits the number of edges grows linearly with N.[2] All four Trotter error coefficients considered in this work are linear in $|E|$ and therefore also linear in N: $\alpha_1 \propto |E|$, $\alpha_2 \propto |E|$, $\alpha_4 \propto |E|$, and $\alpha_6 \propto |E|$.

Substituting $\alpha_p \propto N$ into Eqs. (39)–(42) gives the scaling of the optimal number of Trotter steps with system size:

$$r_1^* \propto N, \qquad r_2^* \propto \sqrt{N}, \qquad r_4^* \propto N^{1/4}, \qquad r_6^* \propto N^{1/6}. \tag{47}$$

The step duration $t_{\text{step}}^{(p)}$ depends on N only through $\chi'(G)$, which is bounded above by $d_{\max} + 1$ and therefore constant for any fixed 2D lattice family. The total energy per experiment is consequently dominated by $r_p^* \, t_{\text{step}}^{(p)}$, and assuming that $t_{\text{step}}^{(p)}$ stays constant with N,

$$\frac{E_{\text{digital}}^{(p)}}{E_{\text{analog}}} \;\propto\; G_p \, N^{1/p} \;\sim\; 5^{p/2} \, N^{1/p}, \tag{48}$$

where the prefactor $G_p \sim 5^{p/2}$ comes from the exponential growth of gates per Trotter step with the order p derived in Section 2.5. Figure 2 shows the full energy curves. At $N = 25$ the optimum is fourth order, as expected for $p^* \approx 3.5$, with the digital cost 90× that of analog. In all cases the analog advantage *grows* with N. The energy comparison reinforces the conclusions

[2] $|E| = 2L(L-1) = 2N - 2\sqrt{N} \to 2N$.

drawn from the gate-count and fidelity analyses. Digital quantum simulation is simultaneously limited by runtime, precision, and energy consumption. While higher-order product formulas can reduce the gate count, the required fidelities, and the energy cost, this advantage does not continue indefinitely. Beyond the optimal order p^* the exponential growth of per-step gates (G_p) overtakes the $N^{1/p}$ shrinkage of r^*, and the total cost begins to grow again with p. Even at the optimum, the resulting circuits remain two to four orders of magnitude more expensive than the native analog evolution. The most efficient digital decomposition at $N = 25$ (fourth order) narrows the energy gap to a factor of $\sim$90, with both approaches costing less than one cent per experiment. Nevertheless, the gap widens with system size, as $N^{1/4}$ for S_4 and $N^{1/6}$ for S_6, and the digital approach still requires gate fidelities three to six orders of magnitude beyond current hardware. For problems that map naturally onto the hardware Hamiltonian, analog quantum simulation provides a more resource-efficient implementation in all three dimensions: **runtime, energy, and direct economic cost.**

7 Conclusion

In this work, we have developed a unified framework to compare the time, accuracy, and energy requirements of Hamiltonian time evolution using product formulas of first, second, fourth and sixth order against analog quantum simulation.

Our analysis shows that, for a simple but representative benchmark task, the time evolution of the transverse-field Ising model on several lattices, it is *not currently possible* to achieve the same precision (within a 5% error budget) on a digital quantum computer that can be obtained directly on an analog quantum computer. For only $1\,\mu$s of evolution on all lattices described, all product-formula decompositions considered here (first, second, fourth and sixth order) require circuit runtimes that exceed the coherence times of state-of-the-art multi-qubit superconducting processors by one to three orders of magnitude. Equivalently, attaining the target precision demands two-qubit gate error rates of $\epsilon_{2q} \sim 10^{-10}$–$10^{-7}$, three to six orders of magnitude below current NISQ hardware capabilities. Both bounds place accurate digital simulation in the *fault-tolerant* regime: high-accuracy digital quantum simulation, even of the simplest Hamiltonian dynamics, will require quantum error correction, with its associated overhead in qubit count, control complexity, and energy consumption.

Even under the assumption that fault-tolerant digital quantum computers *are* available, analog quantum computers retain a substantial advantage on this class of problems. For the same benchmark, the analog approach achieves the target dynamics in $7\,\mu$s compared to $\sim$0.63 ms for the best digital decomposition (fourth-order Trotter), a factor of $\sim 90\times$ in both runtime and energy. Therefore, analog quantum simulation remains more feasible than its digital counterpart in all three dimensions analysed here: *time, energy, and economic cost.*

This analysis focuses on current digital quantum simulation methods. While other techniques, such as Quantum Signal Processing (QSP), Quantum Single Value Transformation (QSVT) or Qubitization [23–26] will become viable in the fault-tolerant regime, evaluating them is left for future work. Specifically, future studies must determine whether these emerging methods can close the runtime and energy gaps between analog and digital simulations identified in this study. However, digital quantum computers will always face inherent errors, as they must approximate continuous physical processes, such as Hamiltonian evolution, into discrete algorithmic steps.

Our results suggest that, even in a future where fault-tolerant digital quantum computing is available, analog quantum platforms will continue to play an important and complementary role for a broad class of problems centred on Hamiltonian time evolution, including many-body quantum simulation, adiabatic quantum computation, quantum annealing, and quantum reservoir computing.

References

[1] Richard P. Feynman. Simulating physics with computers. *International Journal of Theoretical Physics*, 21:467–488, 1982.

[2] I.M. Georgescu, S. Ashhab, and Franco Nori. Quantum simulation. *Reviews of Modern Physics*, 86(1):153–185, March 2014.

[3] M. W. et al Johnson. Quantum annealing with manufactured spins. *Nature*, 473:194–198, 2011. https://doi.org/10.1038/nature10012.

[4] S. et al. Boixo. Evidence for quantum annealing with more than one hundred qubits. *Nature Physics*, 10:218–224, 2014. https://doi.org/10.1038/nphys2900.

[5] Andrew W. Cross, Lev S. Bishop, John A. Smolin, and Jay M. Gambetta. Open quantum assembly language, 2017. https://arxiv.org/abs/1707.03429.

[6] A. et al Kandala. Hardware-efficient variational quantum eigensolver for small molecules and quantum magnets. *Nature*, 549:242–246, 2017. https://doi.org/10.1038/nature23879.

[7] Seth Lloyd. Universal quantum simulators. *Science*, 273:1073–1078, 1996.

[8] Masuo Suzuki. Fractal decomposition of exponential operators. *Physics Letters A*, 146:319–323, 1990.

[9] Morten Kjaergaard, Mollie E. Schwartz, Jochen Braumüller, Philip Krantz, Joel I.-J. Wang, Simon Gustavsson, and William D. Oliver. Superconducting qubits: Current state of play. *Annual Review of Condensed Matter Physics*, 11(1):369–395, March 2020.

[10] Petar Jurcevic, Ali Javadi-Abhari, Lev S Bishop, Isaac Lauer, Daniela F Bogorin, Markus Brink, Lauren Capelluto, Oktay Günlük, Toshinari Itoko, Naoki Kanazawa, Abhinav Kandala, George A Keefe, Kevin Krsulich, William Landers, Eric P Lewandowski, Douglas T McClure, Giacomo Nannicini, Adinath Narasgond, Hasan M Nayfeh, Emily Pritchett, Mary Beth Rothwell, Srikanth Srinivasan, Neereja Sundaresan, Cindy Wang, Ken X Wei, Christopher J Wood, Jeng-Bang Yau, Eric J Zhang, Oliver E Dial, Jerry M Chow, and Jay M Gambetta. Demonstration of quantum volume 64 on a superconducting quantum computing system. *Quantum Science and Technology*, 6(2):025020, March 2021.

[11] Aaron Somoroff, Quentin Ficheux, Raymond A. Mencia, Haonan Xiong, Roman V. Kuzmin, and Vladimir E. Manucharyan. Millisecond coherence in a superconducting qubit, 2021.

[12] Youngkyu Sung, Leon Ding, Jochen Braumüller, Antti Vepsäläinen, Bharath Kannan, Morten Kjaergaard, Ami Greene, Gabriel O. Samach, Chris McNally, David Kim, Alexander Melville, Bethany M. Niedzielski, Mollie E. Schwartz, Jonilyn L. Yoder, Terry P. Orlando, Simon Gustavsson, and William D. Oliver. Realization of high-fidelity cz and zz-free iswap gates with a tunable coupler. *Phys. Rev. X*, 11:021058, Jun 2021.

[13] J. Stehlik, D. M. Zajac, D. L. Underwood, T. Phung, J. Blair, S. Carnevale, D. Klaus, G. A. Keefe, A. Carniol, M. Kumph, Matthias Steffen, and O. E. Dial. Tunable coupling architecture for fixed-frequency transmon superconducting qubits. *Phys. Rev. Lett.*, 127:080505, Aug 2021.

[14] A. Kandala, K. X. Wei, S. Srinivasan, E. Magesan, S. Carnevale, G. A. Keefe, D. Klaus, O. Dial, and D. C. McKay. Demonstration of a high-fidelity cnot gate for fixed-frequency transmons with engineered zz suppression. *Phys. Rev. Lett.*, 127:130501, Sep 2021.

[15] Subir Sachdev. *Quantum Phase Transitions*. Cambridge University Press, 2nd edition, 2011.

[16] IBM Quantum. Scaling for quantum advantage and beyond. https://www.ibm.com/quantum/blog/qdc-2025, 2025.

[17] N. P. de Leon et al. Millisecond lifetimes and coherence times in 2d transmon qubits. *Nature*, 2025. https://doi.org/10.1038/s41586-025-09687-4.

[18] Fabian Marxer et al. Above 99.9% fidelity single-qubit gates, two-qubit gates, and readout in a single superconducting quantum device. https://arxiv.org/abs/2508.16437, 2025.

[19] Rigetti Computing, Inc. Rigetti computing reports fourth quarter and full-year 2025 financial results. https://investors.rigetti.com/news-releases/news-release-details/rigetti-computing-reports-fourth-quarter-and-full-year-2025, March 2026. Accessed: 2026-03-18.

[20] IQM Quantum Computers. Technology and performance benchmarks of IQM's 20-qubit quantum computer: IQM Garnet. https://cdn.prod.website-files.com/6523f13a748909d3e1bbb657/66840c982cc873f725237cbc_IQM%20Garnet%2020Q%20Whitepaper%202024%20sm.pdf, 2024. Median 2-qubit gate fidelity of 99.5%, 20-qubit GHZ state demonstration.

[21] Google Quantum AI. Willow spec sheet. https://quantumai.google/static/site-assets/downloads/willow-spec-sheet.pdf, December 2024. 105-qubit quantum processor with two-qubit gate error of 0.14% (RCS), published December 9, 2024.

[22] U.S. Energy Information Administration. Electric power monthly, table 5.3: Average price of electricity to ultimate customers. https://www.eia.gov/electricity/monthly/epm_table_grapher.php?t=table_5_03, 2025.

[23] D. W. Berry, A. M. Childs, R. Cleve, R. Kothari, and R. D. Somma. Simulating hamiltonian dynamics with a truncated taylor series. *Phys. Rev. Lett.*, 114:090502, 2015.

[24] G. H. Low and I. L. Chuang. Optimal hamiltonian simulation by quantum signal processing. *Phys. Rev. Lett.*, 118:010501, 2017.

[25] G. H. Low and I. L. Chuang. Hamiltonian simulation by qubitization. *Quantum*, 3:163, 2019.

[26] D. Motlagh and N. Wiebe. Generalized quantum signal processing. *PRX Quantum*, 5:020368, 2024.

A Pauli Algebra and Commutator Building Blocks

All calculations below use the commutation relations

$$[X, Y] = 2iZ, \qquad [Y, Z] = 2iX, \qquad [Z, X] = 2iY, \tag{49}$$

and in the opposite order:

$$[Y, X] = -2iZ, \qquad [Z, Y] = -2iX, \qquad [X, Z] = -2iY. \tag{50}$$

Operators on *different* qubits always commute; $X^2 = Y^2 = Z^2 = I$. The single-qubit products that recur below are

$$ZX = iY, \quad XZ = -iY, \quad ZY = -iX, \quad YZ = iX, \quad XY = iZ, \quad YX = -iZ. \tag{51}$$

For Hermitian operators A, B, the commutator $[A, B]$ is anti-Hermitian. Repeated commutators therefore alternate:

$$\text{depth-}k \text{ nested commutator of Hermitian operators } \begin{cases} \text{Hermitian} & k \text{ even}, \\ \text{anti-Hermitian} & k \text{ odd}. \end{cases} \tag{52}$$

Throughout the derivations, we will use the following notation: for a vertex $a \in V$ we write $d_a := \deg(a)$ and $N(a)$ for its open neighbourhood. For an edge $(i, j) \in E$ we write

$$\Delta_{ij} := |N(i) \cap N(j)| \tag{53}$$

for the number of common neighbours of i and j.

B Calculation of α_2

The second-order Trotter error coefficient is

$$\alpha_2 = \|[H_X, [H_X, H_{ZZ}]]\| + \tfrac{1}{2}\|[H_{ZZ}, [H_{ZZ}, H_X]]\| = \|C_{XX}\| + \tfrac{1}{2}\|C_{ZZ}\|. \tag{54}$$

First term: $C_{XX} = [H_X, [H_X, H_{ZZ}]]$

Expanding edge by edge, the inner commutator $[X_{v'}, Z_i Z_j]$ is non-zero only when v' is an endpoint of (i, j):

$$v' = i: \quad [X_i, Z_i Z_j] = -2iY_i Z_j, \tag{55}$$

$$v' = j: \quad [X_j, Z_i Z_j] = -2iZ_i Y_j. \tag{56}$$

The outer commutator $\sum_v [X_v,\ Y_i Z_j + Z_i Y_j]$ receives contributions only from $v \in \{i, j\}$:

$$\sum_v [X_v,\ Y_i Z_j + Z_i Y_j] = 4i(Z_i Z_j - Y_i Y_j). \tag{57}$$

Assembling with the prefactors:

$$C_{XX} = [H_X, [H_X, H_{ZZ}]] = 8Jh^2 \sum_{(i,j)\in E} (Z_i Z_j - Y_i Y_j). \tag{58}$$

Using $\|Z_i Z_j - Y_i Y_j\| \le 2$:

$$\|C_{XX}\| \le 16|Jh^2| \cdot |E|. \tag{59}$$

Second term: $C_{ZZ} = [H_{ZZ}, [H_{ZZ}, H_X]]$

Starting from $[H_{ZZ}, H_X] = 2iJh\sum_{(i,j)\in E}(Y_iZ_j + Z_iY_j)$, the outer commutator $[H_{ZZ}, \cdot]$ contributes only when the outer edge shares a vertex with the inner edge. After collecting all cases (same edge, edge sharing one vertex):

$$C_{ZZ} = 4J^2h \sum_{(i,j)\in E} \left[X_i + X_j + \sum_{\substack{m\sim i \\ m\neq j}} X_iZ_mZ_j + \sum_{\substack{m\sim j \\ m\neq i}} Z_iX_jZ_m \right]. \tag{60}$$

Using the triangle inequality and the handshaking lemma $\sum_{(i,j)}(\deg i + \deg j) \leq 2d_{\max}|E|$:

$$\|C_{ZZ}\| \leq 8|J^2h| \cdot d_{\max}|E|. \tag{61}$$

Combining:

$$\alpha_2 \leq 16|Jh^2| \cdot |E| + 4|J^2h| \cdot d_{\max}|E| = 4|Jh| \cdot |E|\,(4|h| + |J|\,d_{\max}). \tag{62}$$

C Calculation of α_4

The fourth-order Trotter error coefficient α_4 is bounded by a linear combination of norms of all depth-4 nested commutators of H_{ZZ} and H_X:

$$\alpha_4 \leq \sum_{k=1}^{8} |d_k| \cdot \|\mathbf{P_k}\|, \tag{63}$$

where d_k are *universal numerical constants* determined by the Suzuki parameters s_0, s_1 through the Baker–Campbell–Hausdorff (BCH) expansion of S_4 (see Section C.10 below for the full derivation of these coefficients). The sum runs over 8 independent patterns rather than 16 because the identity $\mathbf{P_{17-k}} = -\mathbf{P_k}$ (from $[H_X, H_{ZZ}] = -[H_{ZZ}, H_X]$) allows the 16-pattern decomposition to be simplified:

$$\sum_{k=1}^{16} |c_k|\|\mathbf{P_k}\| = \sum_{k=1}^{8} (|c_k| + |c_{17-k}|)\|\mathbf{P_k}\| \;\geq\; \sum_{k=1}^{8} |d_k|\|\mathbf{P_k}\|, \tag{64}$$

where $d_k = c_k - c_{17-k}$ and the inequality follows from the triangle inequality in reverse.

Writing Z for H_{ZZ} and X for H_X, there are $2^4 = 16$ depth-4 patterns $\mathbf{P_1}, \ldots, \mathbf{P_{16}}$. The antisymmetry of the innermost commutator reduces the number of independent patterns from 16 to 8.

C.1 Symmetry Reductions

Since $[H_X, H_{ZZ}] = -[H_{ZZ}, H_X]$, replacing the innermost commutator negates the entire pattern:

$$[A_1, [A_2, [A_3, [A_4, [H_{ZZ}, H_X]]]]] = -[A_1, [A_2, [A_3, [A_4, [H_X, H_{ZZ}]]]]]. \tag{65}$$

Patterns 1–8 have innermost $[H_X, H_{ZZ}]$; patterns 9–16 have innermost $[H_{ZZ}, H_X]$. Consequently

$$\begin{aligned} \mathbf{P_9} &= -\mathbf{P_8}, \quad \mathbf{P_{10}} = -\mathbf{P_7}, \\ \mathbf{P_{11}} &= -\mathbf{P_6}, \quad \mathbf{P_{12}} = -\mathbf{P_5}, \\ \mathbf{P_{13}} &= -\mathbf{P_4}, \quad \mathbf{P_{14}} = -\mathbf{P_3}, \\ \mathbf{P_{15}} &= -\mathbf{P_2}, \quad \mathbf{P_{16}} = -\mathbf{P_1}. \end{aligned} \tag{66}$$

It suffices to compute $\mathbf{P_1}, \ldots, \mathbf{P_8}$ only.

C.2 Pattern 1: $\mathrm{ad}^4_{H_X}(H_{ZZ})$

Applying $[H_X, \cdot]$ to C_{XX}, and using the result of Eq. (58) restricted to a single edge:

$$[H_X,\, Z_iZ_j - Y_iY_j] = h(-2iY_iZ_j - 2iZ_iY_j) - h(2iZ_iY_j + 2iY_iZ_j) = -4ih(Y_iZ_j + Z_iY_j). \quad (67)$$

Therefore:

$$\mathrm{ad}^3_{H_X}(H_{ZZ}) = [H_X, C_{XX}] = 8Jh^2 \cdot (-4ih) \sum_{(i,j)\in E} (Y_iZ_j + Z_iY_j) = -32iJh^3 \sum_{(i,j)\in E} (Y_iZ_j + Z_iY_j). \quad (68)$$

Comparing with $C_1 = 2iJh \sum (Y_iZ_j + Z_iY_j)$, we obtain the following proportionality:

$$\mathrm{ad}^3_{H_X}(H_{ZZ}) = -16h^2\, C_1. \quad (69)$$

This relation, together with Eq. (67), shows that $\mathrm{ad}^k_{H_X}(H_{ZZ})$ oscillates with period 2 between the operators $\sum (Z_iZ_j - Y_iY_j)$ (even k) and $\sum (Y_iZ_j + Z_iY_j)$ (odd k), with the support remaining strictly 2-body (a single edge) for all k.

Applying $[H_X, \cdot]$ once more to Eq. (69):

$$\mathbf{P_1} = \mathrm{ad}^4_{H_X}(H_{ZZ}) = -32iJh^3 \cdot (-4ih) \sum_{(i,j)\in E} (Z_iZ_j - Y_iY_j) = 128Jh^4 \sum_{(i,j)\in E} (Z_iZ_j - Y_iY_j). \quad (70)$$

$$\mathbf{P_1} = [H_X, [H_X, [H_X, [H_X, H_{ZZ}]]]] = 128Jh^4 \sum_{(i,j)\in E} (Z_iZ_j - Y_iY_j). \qquad \|\mathbf{P_1}\| \le 256\,|Jh^4| \cdot |E|.$$

C.3 Pattern 2: $[H_{ZZ}, \mathrm{ad}^3_{H_X}(H_{ZZ})]$

Using the proportionality Eq. (69) and then the depth-2 result Eq. (60) in one step:

$$\mathbf{P_2} = [H_{ZZ},\, -16h^2 C_1] = -16h^2\, [H_{ZZ},\, [H_{ZZ}, H_X]] = -16h^2\, C_{ZZ}. \quad (71)$$

$$\mathbf{P_2} = [H_{ZZ}, [H_X, [H_X, [H_X, H_{ZZ}]]]]$$
$$= -64J^2h^3 \sum_{(i,j)\in E} \left[X_i + X_j + \sum_{\substack{m\sim i \\ m\neq j}} X_iZ_mZ_j + \sum_{\substack{m\sim j \\ m\neq i}} Z_iX_jZ_m \right].$$

$\|\mathbf{P_2}\| = 16h^2 \|C_{ZZ}\| \le 128\,|J^2h^3| \cdot d_{\max}|E|.$

C.4 Patterns 3 and 4

First we need $C_{ZXX} = [H_{ZZ}, C_{XX}]$. From C_{XX} (Eq. (58)):

$$C_{ZXX} = J \sum_{(k,l)\in E} \sum_{(i,j)\in E} [Z_kZ_l,\; 8Jh^2(Z_iZ_j - Y_iY_j)]. \quad (72)$$

For fixed inner edge (i,j), the outer edge (k,l) contributes only when it shares a vertex with (i,j).

Case: outer edge $(k,l)=(i,n)$, $n\neq j$.

$$\begin{aligned}[Z_iZ_n,\ Z_iZ_j-Y_iY_j] &= [Z_i,Z_i]Z_nZ_j-[Z_i,Y_i]Z_nY_j\\ &= 0-(-2iX_i)Z_nY_j = 2iX_iZ_nY_j. \end{aligned}\tag{73}$$

By $i\leftrightarrow j$: outer edge (j,n), $n\neq i$ gives $2iY_iX_jZ_n$ (after relabelling).

Case: outer edge $(k,l)=(i,j)$ (same edge).

$$[Z_iZ_j,\ Z_iZ_j-Y_iY_j] = 0-[Z_iZ_j,\ Y_iY_j] = [Y_i,Z_i]Y_jZ_j+Z_iY_i[Y_j,Z_j] = 0,\tag{74}$$

since $[Z_iZ_j,Y_iY_j]=(ZY)_i(ZY)_j-(YZ)_i(YZ)_j=(iX)_i(iX)_j-(-iX)_i(-iX)_j=-X_iX_j-(-X_iX_j)=0$.

Collecting (with prefactor $8J^2h^2$ and extra $2i$ from each Pauli comm):

$$C_{ZXX}=16iJ^2h^2\sum_{(i,j)\in E}\Big[\sum_{\substack{n\sim i\\ n\neq j}}X_iY_jZ_n+\sum_{\substack{n\sim j\\ n\neq i}}Y_iX_jZ_n\Big],\tag{75}$$

C.4.1 Derivation of $\mathbf{P_3}$

$\mathbf{P_3}=[H_X,C_{ZXX}]$. From Eq. (75), we apply $[H_X,\cdot]$ to each 3-body term. Only sites $v\in\{j,n\}$ contribute to $[H_X,X_iY_jZ_n]$ since $[X_v,X_i]=0$:

$$v=j:\quad X_i[X_j,Y_j]Z_n=2iX_iZ_jZ_n,\tag{76}$$

$$v=n:\quad X_iY_j[X_n,Z_n]=-2iX_iY_jY_n.\tag{77}$$

So $[H_X,X_iY_jZ_n]=2ih\,X_i(Z_jZ_n-Y_jY_n)$. By $i\leftrightarrow j$: $[H_X,Y_iX_jZ_n]=2ih\,X_j(Z_iZ_n-Y_iY_n)$. Assembling:

$$\begin{aligned}\mathbf{P_3}=[H_X,C_{ZXX}] &= 16iJ^2h^2\cdot 2ih\sum_{(i,j)}\Big[\sum_{\substack{n\sim i\\ n\neq j}}X_i(Z_jZ_n-Y_jY_n)+\sum_{\substack{n\sim j\\ n\neq i}}X_j(Z_iZ_n-Y_iY_n)\Big]\\ &= -32J^2h^3\sum_{(i,j)\in E}\Big[\sum_{\substack{n\sim i\\ n\neq j}}X_i(Z_jZ_n-Y_jY_n)+\sum_{\substack{n\sim j\\ n\neq i}}X_j(Z_iZ_n-Y_iY_n)\Big].\end{aligned}\tag{78}$$

C.4.2 Derivation of $\mathbf{P_4}$

Using $[H_{ZZ},[H_X,H_{ZZ}]]=-C_{ZZ}$, so $\mathbf{P_4}=[H_X,[H_X,-C_{ZZ}]]=-[H_X,[H_X,C_{ZZ}]]$. We first compute $[H_X,C_{ZZ}]$. Only the 3-body terms in C_{ZZ} contribute since $[H_X,X_v]=0$. For $X_iZ_mZ_j$ (with $m\sim i$, $m\neq j$), only $v\in\{m,j\}$:

$$v=m:\quad X_i[X_m,Z_m]Z_j=-2iX_iY_mZ_j,\tag{79}$$

$$v=j:\quad X_iZ_m[X_j,Z_j]=-2iX_iZ_mY_j.\tag{80}$$

By $i\leftrightarrow j$: $[H_X,Z_iX_jZ_m]=-2ih\,X_j(Y_iZ_m+Z_iY_m)$. Collecting (let D denote the sum of these XYZ-type terms):

$$[H_X,C_{ZZ}]=4J^2h\cdot(-2ih)\,D=-8iJ^2h^2\,D.\tag{81}$$

Applying $[H_X,\cdot]$ again. For $X_iY_mZ_j+X_iZ_mY_j$ (with $m\sim i$, $m\neq j$), only $v\in\{m,j\}$:

$$[H_X,X_iY_mZ_j]:\quad v=m:2iX_iZ_mZ_j;\quad v=j:-2iX_iY_mY_j.\quad\Rightarrow\quad 2ih\,X_i(Z_mZ_j-Y_mY_j),\tag{82}$$

$$[H_X,X_iZ_mY_j]:\quad v=m:-2iX_iY_mY_j;\quad v=j:2iX_iZ_mZ_j.\quad\Rightarrow\quad 2ih\,X_i(Z_mZ_j-Y_mY_j).\tag{83}$$

So $[H_X, X_iY_mZ_j + X_iZ_mY_j] = 4ih\, X_i(Z_mZ_j - Y_mY_j)$; by $i \leftrightarrow j$: $[H_X, X_j(Y_iZ_m + Z_iY_m)] = 4ih\, X_j(Z_iZ_m - Y_iY_m)$. Assembling:

$$\mathbf{P_4} = -[H_X, -8iJ^2h^2\, D] = 8iJ^2h^2 \cdot 4ih \sum_{(i,j)} \Big[\sum_{\substack{m\sim i \\ m\neq j}} X_i(Z_mZ_j - Y_mY_j) + \sum_{\substack{m\sim j \\ m\neq i}} X_j(Z_iZ_m - Y_iY_m) \Big]$$

$$= -32J^2h^3 \sum_{(i,j)\in E} \Big[\sum_{\substack{m\sim i \\ m\neq j}} X_i(Z_mZ_j - Y_mY_j) + \sum_{\substack{m\sim j \\ m\neq i}} X_j(Z_iZ_m - Y_iY_m) \Big]. \tag{84}$$

C.4.3 The Identity $\mathbf{P_3} = \mathbf{P_4}$

Comparing Eqs. (78) and (84) term by term for a fixed edge (i, j), we notice:

- *First sum.* $\mathbf{P_3}$ has $\sum_{n\sim i, n\neq j} X_i(Z_jZ_n - Y_jY_n)$ and $\mathbf{P_4}$ has $\sum_{m\sim i, m\neq j} X_i(Z_mZ_j - Y_mY_j)$. Since Z_j and Z_n act on different qubits they commute, so $Z_jZ_n = Z_nZ_j = Z_mZ_j$ (setting $m = n$), and the summation index sets coincide.
- *Second sum.* The same argument with $i \leftrightarrow j$ applies.

Therefore $\mathbf{P_3} = \mathbf{P_4}$ holds for any graph and any coupling constants.

$$\mathbf{P_3} = \mathbf{P_4} = [H_X, [H_{ZZ}, [H_X, [H_X, H_{ZZ}]]]] = [H_X, [H_X, [H_{ZZ}, [H_X, H_{ZZ}]]]]$$
$$= -32J^2h^3 \sum_{(i,j)\in E} \Big[\sum_{\substack{n\sim i \\ n\neq j}} X_i(Z_jZ_n - Y_jY_n) + \sum_{\substack{n\sim j \\ n\neq i}} X_j(Z_iZ_n - Y_iY_n) \Big].$$

Using $\|Z_jZ_n - Y_jY_n\| = 2$ and counting neighbours: $\|\mathbf{P_3}\| = \|\mathbf{P_4}\| \leq 128\,|J^2h^3| \cdot (d_{\max} - 1)|E|$.

C.5 Pattern 5

The pattern under study is

$$\mathbf{P_5} = \big[H_{ZZ}, [H_{ZZ}, [H_X, [H_X, H_{ZZ}]]]\big] = [H_{ZZ}, C_{ZXX}]. \tag{85}$$

We use as building block the result from C_{ZXX} (Eq. 75).

$$C_{ZXX} = 16iJ^2h^2 \sum_{(i,j)\in E} \Big[\sum_{\substack{n\sim i \\ n\neq j}} X_iY_jZ_n + \sum_{\substack{n\sim j \\ n\neq i}} Y_iX_jZ_n \Big], \tag{86}$$

C.5.1 Step 1: $[H_{ZZ},\, X_iY_jZ_n]$ and $[H_{ZZ},\, Y_iX_jZ_n]$

We fix three distinct sites i, j, n with $(i, j) \in E$, $(i, n) \in E$ and $j \neq n$. The inner operator $X_iY_jZ_n$ has support $\{i, j, n\}$. Define

$$\delta_{jn} := [(j, n) \in E] \tag{87}$$

i.e. the indicator of whether the three sites form a triangle.
We compute $[H_{ZZ},\, X_iY_jZ_n] = J \sum_{(k,l)\in E} [Z_kZ_l,\, X_iY_jZ_n]$ case by case in (k, l).

Both endpoints in $\{i, j, n\}$. There are at most three subcases.

$(k, l) = (i, j)$ *(always in E).* Direct calculation gives $Z_iZ_j \cdot X_iY_jZ_n = (Z_iX_i)(Z_jY_j)Z_n = (iY_i)(-iX_j)Z_n = Y_iX_jZ_n$, and $X_iY_jZ_n \cdot Z_iZ_j = (X_iZ_i)(Y_jZ_j)Z_n = (-iY_i)(iX_j)Z_n = Y_iX_jZ_n$. Hence $[Z_iZ_j,\, X_iY_jZ_n] = 0$.

$(k, l) = (i, n)$ *(always in E, since $n \sim i$).* Now $Z_n^2 = I$ and Y_j commutes with Z_iZ_n, so $[Z_iZ_n,\, X_iY_jZ_n] = [Z_i, X_i]\, Y_j\, Z_n^2 = (2iY_i)Y_j = +2iY_iY_j$.

$(k, l) = (j, n)$ *(only if $\delta_{jn} = 1$).* Similarly X_i commutes with Z_jZ_n and $Z_n^2 = I$, giving $[Z_jZ_n,\, X_iY_jZ_n] = X_i[Z_j, Y_j]Z_n^2 = -2iX_iX_j$.

One endpoint in $\{i, j, n\}$, the other a new vertex p. Let $p \notin \{i, j, n\}$. The site p contributes only an outer Z_p factor. The commutator collapses to one site.

Endpoint i. For $(k, l) = (i, p)$ with $p \sim i$, $p \neq j, n$:

$$[Z_iZ_p,\, X_iY_jZ_n] = Z_p\,[Z_i,\, X_i]\,Y_jZ_n = +2i\,Y_iY_jZ_nZ_p. \tag{88}$$

Endpoint j. For $(k, l) = (j, p)$ with $p \sim j$, $p \neq i, n$:

$$[Z_jZ_p,\, X_iY_jZ_n] = Z_p\,X_i[Z_j,\, Y_j]\,Z_n = -2i\,X_iX_jZ_nZ_p. \tag{89}$$

Endpoint n. For $(k, l) = (n, p)$ with $p \sim n$, $p \neq i, j$: $[Z_nZ_p,\, X_iY_jZ_n] = X_iY_j[Z_nZ_p,\, Z_n] = 0$, since Z_n commutes with Z_nZ_p.

Defining the truncated Z-sums

$$S_{i;jn} := \sum_{\substack{p\sim i\\ p\neq j,n}} Z_p, \qquad S_{j;in} := \sum_{\substack{p\sim j\\ p\neq i,n}} Z_p. \tag{90}$$

Combining all cases,

$$[H_{ZZ},\, X_iY_jZ_n] = 2iJ\{Y_iY_j \,-\, \delta_{jn}\,X_iX_j \,+\, Y_iY_j\,Z_n\,S_{i;jn} \,-\, X_iX_j\,Z_n\,S_{j;in}\}\,. \tag{91}$$

The analogue expression for $n \sim j$, $n \neq i$ follows by exchanging $i \leftrightarrow j$ throughout:

$$[H_{ZZ},\, Y_iX_jZ_n] = 2iJ\{Y_iY_j \,-\, \delta_{in}\,X_iX_j \,+\, Y_iY_j\,Z_n\,S_{j;in} \,-\, X_iX_j\,Z_n\,S_{i;jn}\}\,. \tag{92}$$

C.5.2 Step 2: Two and four body parts

Assembling with the constants

$$\mathbf{P_5} = [H_{ZZ},\, D] = 16\,iJ^2h^2 \sum_{(i,j)\in E} \Big[\sum_{\substack{n\sim i\\ n\neq j}} [H_{ZZ},\, X_iY_jZ_n] + \sum_{\substack{n\sim j\\ n\neq i}} [H_{ZZ},\, Y_iX_jZ_n]\Big]. \tag{93}$$

Substituting (91)–(92) and using $16i \cdot 2i = -32$, the prefactor becomes $-32\,J^3h^2$:

$$\mathbf{P_5} = -32\,J^3h^2 \sum_{(i,j)\in E} \Big(\mathcal{T}_{ij}^{(2)} + \mathcal{T}_{ij}^{(4)}\Big), \tag{94}$$

where the per-edge contributions split into a 2-body and a 4-body part.

Two-body part. Summing the constant terms (independent of $S_{\cdot;\cdot}$) over n: the Y_iY_j piece accumulates $|N(i) \setminus \{j\}| = d_i - 1$ contributions from the first sum and $d_j - 1$ from the second, giving a coefficient $d_i + d_j - 2$. The $-X_iX_j\,\delta$ piece accumulates

$$-X_iX_j \sum_{\substack{n\sim i\\ n\neq j}} \delta_{jn} - X_iX_j \sum_{\substack{n\sim j\\ n\neq i}} \delta_{in} = -2\Delta_{ij}\, X_iX_j, \tag{95}$$

since both sums count the common neighbours of i and j. $\Delta_{ij} := |N(i) \cap N(j)|$ is defined precisely as the number of common neighbours of i and j. Hence

$$\boxed{\mathcal{T}^{(2)}_{ij} = (d_i + d_j - 2)\, Y_iY_j \;-\; 2\,\Delta_{ij}\, X_iX_j.} \tag{96}$$

Four-body part. The 4-body contributions per edge come in four blocks, two with Y_iY_j and two with X_iX_j as the edge factor:

$$\mathcal{Q}^{YY}_{ij} = Y_iY_j \sum_{\substack{n\sim i\\ n\neq j}} Z_n\, S_{i;jn} + Y_iY_j \sum_{\substack{n\sim j\\ n\neq i}} !Z_n\, S_{j;in}, \tag{97}$$

$$\mathcal{Q}^{XX}_{ij} = X_iX_j \sum_{\substack{n\sim i\\ n\neq j}} Z_n\, S_{j;in} + X_iX_j \sum_{\substack{n\sim j\\ n\neq i}} Z_n\, S_{i;jn}. \tag{98}$$

Expanding $S_{\cdot;\cdot}$ explicitly,

$$\mathcal{Q}^{YY}_{ij} = Y_iY_j \sum_{\substack{n\sim i\\ n\neq j}} \sum_{\substack{p\sim i\\ p\neq j,n}} Z_nZ_p + Y_iY_j \sum_{\substack{n\sim j\\ n\neq i}} \sum_{\substack{p\sim j\\ p\neq i,n}} Z_nZ_p, \tag{99}$$

$$\mathcal{Q}^{XX}_{ij} = X_iX_j \sum_{\substack{n\sim i\\ n\neq j}} \sum_{\substack{p\sim j\\ p\neq i,n}} Z_nZ_p + X_iX_j \sum_{\substack{n\sim j\\ n\neq i}} \sum_{\substack{p\sim i\\ p\neq j,n}} Z_nZ_p. \tag{100}$$

Hence

$$\boxed{\mathcal{T}^{(4)}_{ij} = \mathcal{Q}^{YY}_{ij} - \mathcal{Q}^{XX}_{ij}.} \tag{101}$$

Combining (94), (96) and (101) we obtain the final closed form of $\mathbf{P_5}$.

$$\mathbf{P_5} = -32\, J^3h^2 \sum_{(i,j)\in E} \Big[(d_i{+}d_j{-}2)\, Y_iY_j - 2\Delta_{ij}\, X_iX_j + \mathcal{Q}^{YY}_{ij} - \mathcal{Q}^{XX}_{ij}\Big]. \tag{102}$$

C.5.3 Step 4: Operator-norm bound

Each of the operators Y_iY_j, X_iX_j, $Y_iY_jZ_nZ_p$, $X_iX_jZ_nZ_p$ is a tensor product of single-qubit Paulis and hence has operator norm 1. The triangle inequality applied to Eq. (102) requires counting the number of summands per edge.

For a fixed edge $(i, j) \in E$:

Source	Number of unit-norm terms
$(d_i + d_j - 2)\, Y_i Y_j$	$d_i + d_j - 2$
$2\Delta_{ij}\, X_i X_j$	$2\Delta_{ij}$
$\mathcal{Q}_{ij}^{YY}$	$(d_i - 1)(d_i - 2) + (d_j - 1)(d_j - 2)$
$\mathcal{Q}_{ij}^{XX}$	$2(d_i - 1)(d_j - 1) - 2\Delta_{ij}$

The third row counts ordered pairs (n, p) with $n, p \in N(i) \setminus \{j\}$ and $p \neq n$ (and the analogous sum at j). The fourth row counts pairs (n, p) with $n \in N(i) \setminus \{j\}$ and $p \in N(j) \setminus \{i, n\}$: there are $(d_i - 1)(d_j - 1)$ unrestricted ordered pairs. Δ_{ij} of them have $p = n$ and must be removed. The factor 2 is because the same combinatorics arises again from the $n \sim j$ side.
Adding the second and fourth rows, the Δ_{ij} contributions cancel

$$2\Delta_{ij} \; + \; [\,2(d_i{-}1)(d_j{-}1) - 2\Delta_{ij}\,] \; = \; 2(d_i{-}1)(d_j{-}1). \tag{103}$$

Summing all four contributions:

$$\begin{aligned} &(d_i + d_j - 2) + (d_i - 1)(d_i - 2) + (d_j - 1)(d_j - 2) + 2(d_i - 1)(d_j - 1) \\ &= d_i^2 + d_j^2 + 2d_i d_j - 4d_i - 4d_j + 4 \\ &= (d_i + d_j)^2 - 4(d_i + d_j) + 4 = (d_i + d_j - 2)^2. \end{aligned} \tag{104}$$

$$\|\mathbf{P_5}\| \;\le\; 32\,|J^3h^2| \sum_{(i,j)\in E} (d_i + d_j - 2)^2 \;\le\; 128\,|J^3h^2| \cdot\, (d_{\max} - 1)^2\,|E|. \tag{105}$$

C.6 Pattern 6

The pattern under study is

$$\mathbf{P_6} \;=\; \big[H_X,\, [H_{ZZ},\, [H_{ZZ},\, [H_X, H_{ZZ}]]]\big]. \tag{106}$$

Working from the inside out we recall, from Eq.(60)

$$C_1 := [H_{ZZ}, H_X] = 2iJh \sum_{(i,j)\in E} (Y_i Z_j + Z_i Y_j), \tag{107}$$

$$\begin{aligned} C_{ZZ} &:= [H_{ZZ}, [H_{ZZ}, H_X]] = [H_{ZZ}, C_1] \\ &= 4J^2 h \sum_{(i,j)\in E} \Big[X_i + X_j + \sum_{\substack{m\sim i \\ m\neq j}} X_i Z_m Z_j + \sum_{\substack{m\sim j \\ m\neq i}} Z_i X_j Z_m \Big]. \end{aligned} \tag{108}$$

Since $[H_X, H_{ZZ}] = -C_1$ and $[H_{ZZ}, -C_1] = -C_{ZZ}$,

$$\mathbf{P_6} = [H_X,\, [H_{ZZ},\, -C_{ZZ}]] = -[H_X,\, K], \qquad K := [H_{ZZ}, C_{ZZ}] = \mathrm{ad}^3_{H_{ZZ}}(H_X). \tag{109}$$

The calculation reduces to first computing K, then applying $-\mathrm{ad}_{H_X}$.

C.6.1 Step 1: $K = [H_{ZZ}, C_{ZZ}]$

We need three single-site building blocks. Using $[Z_a, X_a] = 2iY_a$, $[Z_a, Y_a] = -2iX_a$, and $Z_a^2 = I$:

$[H_{ZZ}, X_a]$. $[Z_k Z_l, X_a]$ vanishes unless $a \in \{k, l\}$. For an outer edge $(a, b) \in E$,

$$[Z_a Z_b, X_a] = [Z_a, X_a]\, Z_b = 2i\, Y_a Z_b,$$

so

$$[H_{ZZ}, X_a] = 2iJ\, Y_a \sum_{b\sim a} Z_b. \tag{110}$$

$[H_{ZZ}, X_i Z_m Z_j]$. Since all Z's mutually commute,

$$[Z_k Z_l, X_i Z_m Z_j] = [Z_k Z_l, X_i]\, Z_m Z_j,$$

which is non-zero only when $i \in \{k, l\}$. For an outer edge $(i, b) \in E$,

$$[Z_i Z_b, X_i Z_m Z_j] = 2i Y_i Z_b Z_m Z_j.$$

The choices $b = m$ and $b = j$ collapse via $Z_a^2 = I$:

$$b = m : 2i Y_i Z_m^2 Z_j = 2i Y_i Z_j, \tag{111}$$
$$b = j : 2i Y_i Z_j Z_m Z_j = 2i Y_i Z_m. \tag{112}$$

Hence

$$[H_{ZZ},\, X_i Z_m Z_j] = 2iJ \left[Y_i Z_j + Y_i Z_m + \sum_{\substack{b\sim i \\ b\neq m,j}} Y_i Z_b Z_m Z_j \right]. \tag{113}$$

$[H_{ZZ}, Z_i X_j Z_m]$. By the same argument with $i \leftrightarrow j$,

$$[H_{ZZ},\, Z_i X_j Z_m] = 2iJ \left[Y_j Z_m + Z_i Y_j + \sum_{\substack{b\sim j \\ b\neq i,m}} Z_i Y_j Z_b Z_m \right]. \tag{114}$$

C.6.2 Assembly

Substitute (110)–(114) into the appendix expression (60) for C_{ZZ}, multiplied by $4J^2 h$:

$$\begin{aligned} K = 4J^2 h \sum_{(i,j)} \Big\{ & 2iJ\, Y_i \sum_{a\sim i} Z_a + 2iJ\, Y_j \sum_{a\sim j} Z_a \\ & + \sum_{\substack{m\sim i \\ m\neq j}} 2iJ \Big[Y_i Z_j + Y_i Z_m + \sum_{\substack{b\sim i \\ b\neq m,j}} Y_i Z_b Z_m Z_j \Big] \\ & + \sum_{\substack{m\sim j \\ m\neq i}} 2iJ \Big[Y_j Z_m + Z_i Y_j + \sum_{\substack{b\sim j \\ b\neq i,m}} Z_i Y_j Z_b Z_m \Big] \Big\}. \end{aligned}$$

The 2-body part collects as follows. Splitting $\sum_{a\sim i} Z_a = Z_j + \sum_{a\sim i, a\neq j} Z_a$, the Y_i pieces combine to

$$Y_i Z_j + Y_i \sum_{a\sim i,\, a\neq j} Z_a + (d_i - 1)\, Y_i Z_j + Y_i \sum_{m\sim i,\, m\neq j} Z_m \;=\; d_i\, Y_i Z_j + 2 Y_i \sum_{a\sim i,\, a\neq j} Z_a.$$

Symmetrically for the Y_j pieces. Thus

$$\begin{aligned} K \;=\; 8iJ^3h \sum_{(i,j)\in E} \Big\{ & d_i\, Y_i Z_j + d_j\, Z_i Y_j \\ & + 2Y_i \sum_{a\sim i,\, a\neq j} Z_a + 2Y_j \sum_{a\sim j,\, a\neq i} Z_a \\ & + \sum_{\substack{m\sim i\\ m\neq j}} \sum_{\substack{b\sim i\\ b\neq m,j}} Y_i Z_b Z_m Z_j \\ & + \sum_{\substack{m\sim j\\ m\neq i}} \sum_{\substack{b\sim j\\ b\neq i,m}} Z_i Y_j Z_b Z_m \Big\}. \end{aligned} \tag{115}$$

The 2-body terms live on the original edge (i,j) and on its incident edges (i,a) and (j,a). The 4-body terms live on length-2 walks rooted at i or j.

C.6.3 Step 2: $\mathbf{P_6} = -[H_X, K]$

The map ad_{H_X} acts site-locally and does not enlarge support. The single-site rules

$$[H_X, Y_v] = 2ih\, Z_v, \qquad [H_X, Z_v] = -2ih\, Y_v \tag{116}$$

yield the following building blocks by Leibniz:

Two-body. $[H_X,\, Y_iZ_a] = 2ih(Z_iZ_a - Y_iY_a)$, and likewise $[H_X,\, Z_iY_a] = 2ih(Z_iZ_a - Y_iY_a)$.

Four-body, $YZZZ$ pattern.

$$[H_X,\, Y_iZ_bZ_mZ_j] = 2ih(Z_iZ_bZ_mZ_j - Y_iY_bZ_mZ_j - Y_iZ_bY_mZ_j - Y_iZ_bZ_mY_j). \tag{117}$$

Four-body, $ZYZZ$ pattern.

$$[H_X,\, Z_iY_jZ_bZ_m] = 2ih(Z_iZ_jZ_bZ_m - Y_iY_jZ_bZ_m - Z_iY_jY_bZ_m - Z_iY_jZ_bY_m). \tag{118}$$

Applying (117)–(118) term by term to the four blocks of K in (115) and using $-(8iJ^3h)\cdot(2ih) = +16J^3h^2$:

$$\begin{aligned} \mathbf{P_6} \;=\; 16\,J^3h^2 \sum_{(i,j)\in E} \Big\{ & (d_i + d_j)\,(Z_iZ_j - Y_iY_j) \\ & + 2 \sum_{a\sim i,\, a\neq j} (Z_iZ_a - Y_iY_a) \;+\; 2 \sum_{a\sim j,\, a\neq i} (Z_jZ_a - Y_jY_a) \\ & + \sum_{\substack{m\sim i\\ m\neq j}} \sum_{\substack{b\sim i\\ b\neq m,j}} \big(Z_iZ_bZ_mZ_j - Y_iY_bZ_mZ_j - Y_iZ_bY_mZ_j - Y_iZ_bZ_mY_j\big) \\ & + \sum_{\substack{m\sim j\\ m\neq i}} \sum_{\substack{b\sim j\\ b\neq i,m}} \big(Z_iZ_jZ_bZ_m - Y_iY_jZ_bZ_m - Z_iY_jY_bZ_m - Z_iY_jZ_bY_m\big) \Big\}. \end{aligned} \tag{119}$$

C.6.4 Step 3: Operator-norm bound

Each Pauli string in (119) has operator norm 1. The triangle inequality reduces the bound on $\|\mathbf{P_6}\|$ to a counting argument. For a fixed edge $(i,j) \in E$, contributions to the sum of moduli of coefficients:

Source	Sum of |coefficients| on unit-norm Paulis
$(d_i + d_j)(Z_iZ_j - Y_iY_j)$	$2(d_i + d_j)$
$2\sum_{a\sim i,\, a\neq j}(Z_iZ_a - Y_iY_a)$	$4(d_i - 1)$
$2\sum_{a\sim j,\, a\neq i}(Z_jZ_a - Y_jY_a)$	$4(d_j - 1)$
4-body block from the i-side	$4(d_i - 1)(d_i - 2)$
4-body block from the j-side	$4(d_j - 1)(d_j - 2)$

The four contributions per ordered pair (m,b) in the 4-body blocks each carry coefficient ± 1 in modulus, giving 4 per ordered pair. The number of ordered pairs is $(d_i - 1)(d_i - 2)$ on the i-side and $(d_j - 1)(d_j - 2)$ on the j-side.

Adding the rows of the table:

$$\begin{aligned} R_{ij} &:= 2(d_i + d_j) + 4(d_i - 1) + 4(d_j - 1) + 4(d_i - 1)(d_i - 2) + 4(d_j - 1)(d_j - 2) \\ &= 6(d_i + d_j) - 8 + 4(d_i - 1)(d_i - 2) + 4(d_j - 1)(d_j - 2). \end{aligned} \tag{120}$$

For a regular graph, $d_i = d_j = d$, this collapses to

$$R \;=\; 12d - 8 + 8(d-1)(d-2) \;=\; 8d^2 - 12d + 8 \;=\; 4(2d^2 - 3d + 2). \tag{121}$$

Therefore

$$\|\mathbf{P_6}\| \;\leq\; 16\,|J^3h^2| \sum_{(i,j)\in E} \Big[6(d_i + d_j) - 8 + 4(d_i - 1)(d_i - 2) + 4(d_j - 1)(d_j - 2)\Big], \tag{122}$$

$$\|\mathbf{P_6}\| \;\leq\; 64\,|J^3h^2| \cdot (2d_{\max}^2 - 3d_{\max} + 2)\,|E| \;\leq\; 128\,|J^3h^2| \cdot d_{\max}^2\,|E|, \tag{123}$$

where the last inequality, used to give a clean monomial in $d_{\max}$, is the looser of the two but matches the dominant high-degree behaviour.

C.7 Pattern 7

The pattern

$$\mathbf{P_7} \;=\; \big[H_{ZZ},\, [H_X,\, [H_{ZZ},\, [H_X, H_{ZZ}]]]\big]$$

differs from $\mathbf{P_5} = [H_{ZZ}, [H_{ZZ}, [H_X, [H_X, H_{ZZ}]]]]$ only in the order of the two middle commutators. As a Lie-algebra expression, the identity $\mathbf{P_7} = \mathbf{P_5}$ follows immediately from the Jacobi identity applied to $[H_X, H_{ZZ}]$.

Setting $A := H_X$, $B := H_{ZZ}$, and $X := [A,B] = [H_X, H_{ZZ}]$, the two patterns read

$$\begin{aligned} \mathbf{P_5} &= [B,\, [B,\, [A, X]]], \\ \mathbf{P_7} &= [B,\, [A,\, [B, X]]]. \end{aligned}$$

Their difference is

$$\mathbf{P_5} - \mathbf{P_7} \;=\; [B,\; [B,[A,X]] - [A,[B,X]]]. \tag{124}$$

The Jacobi identity, applied to A, B, X, gives

$$[A,[B,X]] + [B,[X,A]] + [X,[A,B]] \;=\; 0, \tag{125}$$

i.e. (using $[B,[X,A]] = -[B,[A,X]]$ and $[A,B] = X$)

$$[B,[A,X]] - [A,[B,X]] \;=\; [X,[A,B]] \;=\; [X,X] \;=\; 0. \tag{126}$$

Therefore

$$\mathbf{P_5} = \mathbf{P_7} \tag{127}$$

C.8 Pattern 8

The pattern under study reduces to

$$\mathbf{P_8} \;=\; -\mathrm{ad}^4_{H_{ZZ}}(H_X) \;=\; -[H_{ZZ},\, K], \qquad K := \mathrm{ad}^3_{H_{ZZ}}(H_X). \tag{128}$$

The closed-form expression for K was derived in the previous section $\mathbf{P_6}$:

$$K = 8iJ^3h \sum_{(i,j)\in E} \Big\{ d_i\, Y_iZ_j + d_j\, Z_iY_j \;+\; 2Y_i \sum_{\substack{a\sim i\\ a\neq j}} Z_a \;+\; 2Y_j \sum_{\substack{a\sim j\\ a\neq i}} Z_a \;+\; \mathcal{Y}^{(i)}_{ij} + \mathcal{Y}^{(j)}_{ij} \Big\}, \tag{129}$$

where $\mathcal{Y}^{(i)}_{ij} := \sum_{m\sim i, m\neq j} \sum_{b\sim i, b\neq m,j} Y_iZ_bZ_mZ_j$ and $\mathcal{Y}^{(j)}_{ij}$ is the symmetric expression with $i \leftrightarrow j$.

C.8.1 Step 1: Auxiliary commutators with H_{ZZ}

We need $[H_{ZZ}, \cdot\,]$ on each of the four pieces of K in (129). By the structural lemma, all results have active site at $v \in \{i,j\}$ with X_v flipped from the Y_v in K, modulated by neighbour structure.

$[H_{ZZ}, Y_iZ_a]$, with $a \in N(i)$ Active site i. Outer edge $(i,b) \in E$ with $b \sim i$: $[Z_iZ_b,\, Y_iZ_a] = [Z_i, Y_i]Z_bZ_a = -2iX_iZ_bZ_a$. The case $b = a$ collapses via $Z_a^2 = I$:

$$[H_{ZZ},\, Y_iZ_a] \;=\; -2iJ\, X_i \left[1 + \sum_{b\sim i,\, b\neq a} Z_bZ_a \right]. \tag{130}$$

$[H_{ZZ}, Y_iZ_bZ_mZ_j]$, with $b, m \in N(i)\setminus\{j\}$, $b \neq m$ Active site i. Outer edge (i,c) with $c \sim i$. Each of the cases $c \in \{b,m,j\}$ collapses one Z to identity; $c \notin \{b,m,j\}$ adds a fourth Z to the support (yielding a 5-body operator):

$$[H_{ZZ},\, Y_iZ_bZ_mZ_j] \;=\; -2iJ\, X_i \left[Z_mZ_j + Z_bZ_j + Z_bZ_m + \sum_{\substack{c\sim i\\ c\notin\{b,m,j\}}} Z_cZ_bZ_mZ_j \right]. \tag{131}$$

The symmetric building block $[H_{ZZ},\, Z_iY_jZ_bZ_m]$ with $b, m \in N(j)\setminus\{i\}$, $b \neq m$, follows by interchanging $i \leftrightarrow j$.

C.8.2 Step 2: Assembly of $L = [H_{ZZ}, K]$

We now collect the contributions from each block of K in (129), all with the common prefactor $8iJ^3h$ and an additional $-2iJ$ from the inner $[H_{ZZ}, \cdot]$, giving $8iJ^3h \cdot (-2iJ) = 16J^4h$ as the overall factor. Below, all sums are restricted to $a, b, c \in N(i)\setminus\{j\}$ (or $N(j)\setminus\{i\}$ on the symmetric side) and pairwise distinct as indicated.

Contributions on the i-side Substituting (130) and (131):

- From $d_i\, Y_i Z_j$: $\quad -2iJ d_i\, X_i \Big[1 + Z_j \sum_{b\sim i,\, b\neq j} Z_b\Big]$.
- From $2Y_i \sum_{a\sim i,\, a\neq j} Z_a$: $\quad -4iJ\, X_i \Big[(d_i - 1) + Z_j \sum_{a\sim i,\, a\neq j} Z_a + \mathcal{S}_{ij}^{(2)}\Big]$, where $\mathcal{S}_{ij}^{(2)} := \sum_{a,b\sim i,\, a,b\neq j,\, a\neq b} Z_a Z_b$ (ordered double sum).
- From $\mathcal{Y}_{ij}^{(i)}$: $\quad -2iJ\, X_i \Big[2(d_i - 2)\, Z_j \sum_{a\sim i,\, a\neq j} Z_a + \mathcal{S}_{ij}^{(2)} + 6\, Z_j \sum_{T\subset N(i)\setminus\{j\},\, |T|=3} \prod_{t\in T} Z_t\Big]$.

The third bullet uses $\sum_{(m,b)\ \mathrm{ord}} (X_i Z_m Z_j + X_i Z_b Z_j) = 2(d_i - 2) X_i Z_j \sum_a Z_a$, $\sum_{(m,b)\ \mathrm{ord}} X_i Z_b Z_m = X_i \mathcal{S}_{ij}^{(2)}$, and the fact that the 5-body sum $\sum_{(m,b)} \sum_c X_i Z_c Z_b Z_m Z_j$ runs over ordered triples of distinct elements of $N(i)\setminus\{j\}$, of which there are $6\binom{d_i - 1}{3}$ for each 3-subset T.

Combining the three blocks Adding the contributions (multiplied by $8iJ^3h$ to give L, with the $-2iJ/-4iJ$ inner factors), the coefficient of every Pauli of the same shape collects to a particularly clean form. Reading off the coefficient of each Pauli on the i-side:

Pauli shape	**Coefficient (in units of J^4h)**
X_i	$16\big[d_i + 2(d_i - 1)\big] = 16(3d_i - 2)$
$X_i Z_j Z_a$, $a \in N(i)\setminus\{j\}$	$16\big[d_i + 2 + 2(d_i - 2)\big] = 16(3d_i - 2)$
$X_i Z_a Z_b$, $a, b \in N(i)\setminus\{j\}$, $a \neq b$	$16\big[2 + 1\big] = 16 \cdot 3$
$X_i Z_j Z_a Z_b Z_c$, $a, b, c \in N(i)\setminus\{j\}$ distinct	$16 \cdot 6$

Closed form of $\mathbf{P_8}$ Therefore $\mathbf{P_8} = -L$ reads, with all a, b, c ranging over the indicated neighbour sets of i and pairwise distinct:

$$\begin{aligned}\mathbf{P_8} = -16J^4h \sum_{(i,j)\in E} \Big\{ & (3d_i - 2)\, X_i \;+\; (3d_j - 2)\, X_j \\ & + (3d_i - 2)\, X_i Z_j \sum_{a\sim i,\, a\neq j} Z_a \;+\; (3d_j - 2)\, X_j Z_i \sum_{a\sim j,\, a\neq i} Z_a \\ & + 3\, X_i \sum_{\substack{a,b\sim i\\ a,b\neq j\\ a\neq b}} Z_a Z_b \;+\; 3\, X_j \sum_{\substack{a,b\sim j\\ a,b\neq i\\ a\neq b}} Z_a Z_b \\ & + 6\, X_i Z_j \sum_{\substack{T\subset N(i)\setminus\{j\}\\ |T|=3}} \prod_{t\in T} Z_t \;+\; 6\, X_j Z_i \sum_{\substack{T\subset N(j)\setminus\{i\}\\ |T|=3}} \prod_{t\in T} Z_t \Big\}. \end{aligned} \tag{132}$$

In particular, $\mathbf{P_8}$ contains 1-, 3-, and 5-body Pauli strings, all with active X at one of the edge endpoints.

C.8.3 Step 3: Operator-norm bound

For a fixed edge $(i,j) \in E$ and the i-side contribution to the sum of moduli of coefficients on unit-norm Pauli strings:

Pauli shape	**Coefficient**	**Number of strings**
X_i	$3d_i - 2$	1
$X_i Z_j Z_a$ $(a \in N(i)\backslash\{j\})$	$3d_i - 2$	$d_i - 1$
$X_i Z_a Z_b$ (unord. pair $\subset N(i)\backslash\{j\}$)	6	$\binom{d_i-1}{2}$
$X_i Z_j Z_a Z_b Z_c$ $(T \subset N(i)\backslash\{j\}, \lvert T\rvert = 3)$	6	$\binom{d_i-1}{3}$

The factor 6 on the third row comes from the ordered double sum: each unordered pair appears twice, and combined with the coefficient 3 from (132) gives $3 \cdot 2 = 6$. The factor 6 on the fourth row similarly comes from the 6 orderings of each 3-subset combined with the prefactor in (132).

Summing the row totals (coefficient times count) on the i-side and calling the sum $f(d_i)$:

$$\begin{aligned} f(d) \;&:= (3d-2)\cdot 1 + (3d-2)(d-1) + 6\binom{d-1}{2} + 6\binom{d-1}{3} \\ &= (3d-2) + (3d-2)(d-1) + 3(d-1)(d-2) + (d-1)(d-2)(d-3). \end{aligned} \tag{133}$$

Direct expansion gives

$$(3d-2) + (3d^2 - 5d + 2) + (3d^2 - 9d + 6) + (d^3 - 6d^2 + 11d - 6) \;=\; d^3,$$

The triangle inequality on (132) then gives, with $f(d_i) + f(d_j) = d_i^3 + d_j^3$ per edge,

$$\|\mathbf{P_8}\| \;\le\; 16\,|J^4 h| \sum_{(i,j)\in E} \left(d_i^3 + d_j^3\right) \;=\; 16\,|J^4 h| \sum_{v\in V} d_v^4 \;\le\; 32\,|J^4 h| \cdot d_{\max}^3\,|E|. \tag{134}$$

The middle equality uses $\sum_{(i,j)\in E}(d_i^3 + d_j^3) = \sum_v d_v \cdot d_v^3 = \sum_v d_v^4$, and the final inequality uses $d_v \le d_{\max}$ together with $\sum_v d_v = 2|E|$.

C.9 Bounds for α_4

In Table 10 we present all the norm bounds computed for α_4.

Table 10: All 16 depth-4 patterns and their norm bounds. Patterns 9–16 are negatives of 8–1 (antisymmetry $\mathbf{P_{17-k}} = -\mathbf{P_k}$) and have the same norms.

Pattern	Sequence	Norm bound	Method
$\mathbf{P_1}$	$[X,[X,[X,[X,Z]]]]$	$256\,\lvert Jh^4\rvert \cdot \lvert E\rvert$	Direct
$\mathbf{P_2}$	$[Z,[X,[X,[X,Z]]]]$	$128\,\lvert J^2h^3\rvert \cdot d_{\max}\lvert E\rvert$	$-16h^2C_{ZZ}$
$\mathbf{P_3 = P_4}$	$[X,[Z,[X,[X,Z]]]] = [X,[X,[Z,[X,Z]]]]$	$128\,\lvert J^2h^3\rvert \cdot (d_{\max}-1)\lvert E\rvert$	Direct
$\mathbf{P_5 = P_7}$	$[Z,[Z,[X,[X,Z]]]] = [Z,[X,[Z,[X,Z]]]]$	$128\,\lvert J^3h^2\rvert \cdot (d_{\max}-1)^2\lvert E\rvert$	Direct
$\mathbf{P_6}$	$[X,[Z,[Z,[X,Z]]]]$	$128\,\lvert J^3h^2\rvert \cdot d_{\max}^2\lvert E\rvert$	Direct
$\mathbf{P_8}$	$[Z,[Z,[Z,[X,Z]]]]$	$32\,\lvert J^4h\rvert \cdot d_{\max}^3\lvert E\rvert$	Direct
$\mathbf{P_9}$	$[Z,[Z,[Z,[Z,X]]]]$	$32\,\lvert J^4h\rvert \cdot d_{\max}^3\lvert E\rvert$	$-\mathbf{P_8}$
$\mathbf{P_{10}}$	$[X,[Z,[Z,[Z,X]]]]$	$128\,\lvert J^3h^2\rvert \cdot (d_{\max}-1)^2\lvert E\rvert$	$-\mathbf{P_7}$
$\mathbf{P_{11}}$	$[Z,[X,[Z,[Z,X]]]]$	$128\,\lvert J^3h^2\rvert \cdot d_{\max}^2\lvert E\rvert$	$-\mathbf{P_6}$
$\mathbf{P_{12}}$	$[Z,[Z,[X,[Z,X]]]]$	$128\,\lvert J^3h^2\rvert \cdot (d_{\max}-1)^2\lvert E\rvert$	$-\mathbf{P_5}$
$\mathbf{P_{13}}$	$[X,[X,[Z,[Z,X]]]]$	$128\,\lvert J^2h^3\rvert \cdot (d_{\max}-1)\lvert E\rvert$	$-\mathbf{P_4}$
$\mathbf{P_{14}}$	$[Z,[X,[X,[Z,X]]]]$	$128\,\lvert J^2h^3\rvert \cdot (d_{\max}-1)\lvert E\rvert$	$-\mathbf{P_3}$
$\mathbf{P_{15}}$	$[X,[Z,[X,[Z,X]]]]$	$128\,\lvert J^2h^3\rvert \cdot d_{\max}\lvert E\rvert$	$-\mathbf{P_2}$
$\mathbf{P_{16}}$	$[X,[X,[X,[Z,X]]]]$	$256\,\lvert Jh^4\rvert \cdot \lvert E\rvert$	$-\mathbf{P_1}$

C.10 Computation of the BCH Coefficients d_k

The coefficients d_k appearing in the bound Eq. (63) are *universal numerical constants* of the Suzuki fourth-order decomposition Eq. (12). They do not depend on the specific Hamiltonian, graph, or coupling constants, only on the Suzuki parameters s_1 and s_0.

C.10.1 BCH expansion of the Suzuki formula

For any product formula $S(\tau)$ built from matrix exponentials, the matrix logarithm admits an expansion in the free Lie algebra generated by $A := H_X$ and $B := H_{ZZ}$:

$$\ln S_4(\tau) = (A+B)\,\tau + E_5\,\tau^5 + \mathcal{O}(\tau^7), \tag{135}$$

where the τ^3 term vanishes by the Suzuki cancellation condition $4s_1^3 + s_0^3 = 0$, and E_5 is a degree-5 element of the free Lie algebra on two generators. The Trotter error is then

$$\left\| S_4(t/r)^r - e^{(A+B)t} \right\| \;\le\; \|E_5\|\,\frac{t^5}{r^4} + \mathcal{O}\!\left(\frac{t^7}{r^6}\right). \tag{136}$$

The error generator E_5 receives two types of contributions when the five S_2 factors in Eq. (12) are composed via the BCH formula:

1. *Direct terms:* the fifth-order BCH terms of each individual $S_2(s_i\tau)$ factor, weighted by s_i^5.
2. *Cross-terms:* products of lower-order BCH terms from *different* S_2 factors (e.g., first-order $\times$ third-order components), combined through the nested commutator structure of the BCH formula itself.

Both contributions involve products of BCH numerical factors ($\frac{1}{12}$, $\frac{1}{24}$, $\frac{1}{720}$, etc.) with powers of the Suzuki parameters ($s_1^5 \approx 0.012$, $s_0^5 \approx -0.123$, etc.), which is why the resulting coefficients d_k are small ($\sim 10^{-4}$–10^{-3}).

C.10.2 Decomposition into patterns

Since E_5 is a degree-5 Lie element, it can be decomposed in the basis of depth-4 nested commutators of A and B. Due to the identity $\mathbf{P_{17-k}} = -\mathbf{P_k}$, only patterns 1–8 are independent, and

$$E_5 = \sum_{k=1}^{8} d_k \, \mathbf{P_k}, \tag{137}$$

where $d_k = c_k - c_{17-k}$ combines the contributions from both innermost orderings $[A, B]$ and $[B, A]$. Applying the triangle inequality then yields $\|E_5\| \leq \sum_{k=1}^{8} |d_k| \, \|\mathbf{P_k}\| = \alpha_4$.

C.10.3 How to compute the coefficients

The coefficients d_k can be extracted by a purely algebraic computation in the *non-commutative polynomial algebra* generated by two abstract symbols A, B. The procedure is:

1. Represent $\exp(c\,A\,\tau)$ and $\exp(c\,B\,\tau)$ as formal power series in τ, with non-commutative polynomial coefficients, truncated at order 5.
2. Compose the five factors of $S_4(\tau)$ by multiplying these power series (using concatenation as the product of words).
3. Take the formal power-series logarithm $\ln(I+X) = X - X^2/2 + X^3/3 - \cdots$ to obtain $\ln S_4(\tau)$, again truncated at order 5.
4. Read off the coefficient of τ^5: this is E_5, expressed as a non-commutative polynomial in words of length 5.
5. Expand each pattern $\mathbf{P_k}$ as a non-commutative polynomial (e.g., $[A,[A,B]] = A^2B - 2ABA + BA^2$) and solve the linear system $E_5 = \sum d_k \mathbf{P_k}$.

Because A and B are abstract (no matrix representation is needed), this computation is exact and can be carried out with standard linear algebra over $\mathbb{Q}(s_0, s_1)$. The non-commutative polynomial at degree 5 involves at most $2^5 = 32$ distinct words.

D Numerical approximation of α_6

The strategy is to *(i)* fit α_6 directly from the operator-norm error of S_6 on a small reference lattice, *(ii)* rescale to the target lattices assuming a linear scaling with $|E|$ of the bound, and *(iii)* calibrate against the analytical α_4 bounds of Appendix C to keep the conservativeness uniform across the analysis.

D.1 Numerical fit on a small reference lattice

For $H = H_X + H_{ZZ}$ on a 3×3 square TFIM lattice ($n = 9$ qubits, $|E| = 12$, $J = h = 10$) we construct H_X, H_{ZZ} as explicit $2^n \times 2^n$ matrices, evaluate $U_{\text{ex}}(\tau) = e^{-iH\tau}$ via Padé approximation, and assemble $S_6(\tau)$ by composition of matrix exponentials of H_X, H_{ZZ} following the Suzuki

recursion of Eq. (15). The error $E(\tau) = \|S_6(\tau) - U_{\text{ex}}(\tau)\|_{\text{op}}$ is sampled at eight values of $\tau \in [3\times10^{-3}, 2.5\times10^{-2}]$, chosen to keep $E(\tau)$ between $\sim 10^{-11}$ (above floating-point noise) and $\sim 10^{-5}$. We then perform a linear fit in log–log space,

$$\log E(\tau) \;=\; (p+1)\log\tau + \log\alpha_p, \qquad p = 2, 4, 6, \tag{138}$$

which simultaneously yields the leading-order coefficient and a self-consistency check on the convergence order. The output is shown in Table 11.

Table 11: Numerical fit of α_p on the 3×3 square TFIM ($J = h = 10$). The fitted slope reproduces the expected τ^{p+1} scaling to better than 5% in all three cases, validating the leading-order ansatz.

Order p	Fitted slope	Expected $p+1$	α_p (fitted)	$\alpha_p/\lvert E\rvert$
2	2.87	3	7.48×10^{3}	6.24×10^{2}
4	4.90	5	2.79×10^{5}	2.33×10^{4}
6	6.96	7	3.12×10^{6}	2.60×10^{5}

D.2 Extensivity and rescaling to the target lattices

The same locality argument that underlies the α_2 and α_4 bounds applies to α_6. Every depth-k commutator pattern of H_X, H_{ZZ} acts only on a k-radius neighbourhood of one edge, so its operator norm satisfies $\|\mathbf{P_j}\| \le c_j\,|E|$ for some j-dependent geometric constant. Summing over the depth-6 nested commutator patterns and applying the BCH coefficients gives

$$\alpha_6(G) \;=\; \alpha_6^{\text{bulk}}\,|E(G)| \;+\; \mathcal{O}(\partial G), \tag{139}$$

with α_6^{bulk} a chip-independent per-edge constant that depends on J, h and on the local geometry of the lattice (through $d_{\max}$). We adopt $\alpha_6^{\text{bulk}} \equiv \alpha_6^{(3\times3)}/12 = 2.60\times10^5$ from Table 11. This estimate overestimates α_6 on the hexagonal chip ($d_{\max} = 3$ vs. 4 for square; the corresponding ratio of per-edge α_4 values is ~ 0.50 once the corrected $d_{\max}$ dependence of Appendix C is taken into account) and is essentially unbiased on the square chips (4×4 and 5×5 have the same $d_{\max} = 4$ as the reference, with smaller relative boundary).

The 5×5 entry in the α_4 table corresponds to a per-edge coefficient

$$\alpha_4^{\text{bound}}/|E| \;=\; 1.19\times10^7/40 \;=\; 2.99\times10^5,$$

whereas the numerical fit on the same family of square lattices gives $\alpha_4^{\text{num}}/|E| \;=\; 2.33\times10^4$. The slack ratio

$$\text{SLACK} \;\equiv\; \frac{\alpha_4^{\text{bound}}}{\alpha_4^{\text{num}}} \;=\; \frac{2.99\times10^5}{2.33\times10^4} \;\approx\; 12.8 \tag{140}$$

We take it as a proxy for the analogous depth-6 slack and define the bound-style estimate

$$\alpha_6 \;\equiv\; \text{SLACK} \;\times\; \alpha_6^{\text{bulk}} \;\times\; |E| \;=\; 12.8 \;\times\; 2.60\times10^5 \;\times\; |E| \;\approx\; 3.34\times10^6 \;\times\; |E|. \tag{141}$$

E Energy Cost Calculations

This appendix details the formulas and parameters used to compute the energy costs reported in Section 6 and Figure 2. We assume all paradigms share the same structure: energy equals power times runtime. What differs between analog and digital approaches is how the runtime depends on the product-formula order and the system size.

E.1 Common Parameters

Parameter	Symbol	Value
System power (cryo + electronics)	P_{sys}	19 kW
Evolution time	t_{evol}	1 μs
Number of shots	N_{shots}	20 000
Qubit reset time	t_{reset}	5 μs
Measurement time	t_{meas}	1 μs
Two-qubit gate duration	t_{2q}	50 ns
Single-qubit gate duration	t_{1q}	5 ns
Chromatic index (5×5 sq.)	$\chi'(G)$	4
Coupling strengths (μs^{-1})	J, h	10
Total error budget	η	0.05 (5%)
Electricity price		\$0.14/kWh

Table 12: Parameters used in the energy cost calculations.

E.2 Analog Quantum Computing

In the simplified model used here, the reset, evolution, and measurement times are taken to be independent of system size:

$$t_{\text{shot}}^{\text{analog}} = t_{\text{reset}} + t_{\text{evol}} + t_{\text{meas}} = 5 + 1 + 1 = 7\ \mu\text{s}. \tag{142}$$

The total energy over N_{shots} repetitions is

$$E_{\text{analog}} = P_{\text{sys}} \times N_{\text{shots}} \times t_{\text{shot}}^{\text{analog}} = 19\,000 \times 20\,000 \times 7 \times 10^{-6} = 2\,660\ \text{J} \approx 2.66\ \text{kJ}. \tag{143}$$

E.3 Digital Quantum Computing

In the digital approach, the continuous evolution is replaced by a Trotterised circuit. The runtime per shot is

$$t_{\text{shot}}^{\text{digital}} = t_{\text{reset}} + r_p^* \times t_{\text{step}}^{(p)} + t_{\text{meas}}, \tag{144}$$

where r_p^* is the number of Trotter steps determined by the error budget (Eqs. 39–42), and $t_{\text{step}}^{(p)}$ is the wall-clock time of one product-formula step after parallelisation via edge colouring.

Trotter steps. The error budget is split equally: $\epsilon_{\text{Trotter}} = \eta/2 = 0.025$. For the 5×5 lattice ($|E| = 40$, $d_{\max} = 4$, $\chi' = 4$):

$$S_1: \quad r_1^* = \left\lceil \frac{\alpha_1}{\eta} \right\rceil = \left\lceil \frac{16\,000}{0.05} \right\rceil = 320\,000, \tag{145}$$

$$S_2: \quad r_2^* = \left\lceil \sqrt{\frac{\alpha_2}{6\eta}} \right\rceil = \left\lceil \sqrt{\frac{1.28 \times 10^6}{0.30}} \right\rceil = 2\,066, \tag{146}$$

$$S_4: \quad r_4^* = \left\lceil \left(\frac{2\alpha_4}{\eta} \right)^{1/4} \right\rceil = \left\lceil \left(\frac{2 \times 1.19 \times 10^7}{0.05} \right)^{1/4} \right\rceil = 148, \tag{147}$$

$$S_6: \quad r_6^* = \left\lceil \left(\frac{2\alpha_6}{\eta} \right)^{1/6} \right\rceil = \left\lceil \left(\frac{2 \times 1.34 \times 10^8}{0.05} \right)^{1/6} \right\rceil = 42. \tag{148}$$

Step durations. After edge-colouring parallelisation with $\chi' = 4$, the wall-clock time of one Trotter step is (cf. the gate-count table in Section 4):

$$S_1: \quad t_{\text{step}}^{(1)} = 2\chi' t_{2q} + (\chi' + 1)\, t_{1q} = 8 \times 50 + 5 \times 5 = 425 \text{ ns}, \tag{149}$$

$$S_2: \quad t_{\text{step}}^{(2)} = 4\chi' t_{2q} + (2\chi' + 1)\, t_{1q} = 16 \times 50 + 9 \times 5 = 845 \text{ ns}, \tag{150}$$

$$S_4: \quad t_{\text{step}}^{(4)} = 20\chi' t_{2q} + (10\chi' + 5)\, t_{1q} = 80 \times 50 + 45 \times 5 = 4\,225 \text{ ns}, \tag{151}$$

$$S_6: \quad t_{\text{step}}^{(6)} = 100\chi' t_{2q} + (50\chi' + 25)\, t_{1q} = 400 \times 50 + 225 \times 5 = 21\,125 \text{ ns}. \tag{152}$$

The runtime per shot, total time, and energy for each order are:

Table 13: Runtime and active-shot energy estimates for the 5×5 lattice benchmark, using $P_{\text{sys}} = 19\,\text{kW}$ and $N_{\text{shots}} = 20{,}000$.

Order	r^*	$r^* \times t_{\text{step}}$	T_{shot}	T_{total}	E_{total}
S_1	320 000	136.0 ms	136.0 ms	2 720 s	51 682 kJ
S_2	2 066	1.746 ms	1.752 ms	35.0 s	666 kJ
S_4	148	0.625 ms	0.631 ms	12.6 s	240 kJ
S_6	42	0.887 ms	0.893 ms	17.9 s	339 kJ